Matthias Urban

Temperature measurement of CH_4 and H_2 flames with variable O_2 ratios on a flat flame burner using laser absorption spectroscopy and validation through 1D-simulation

Research paper for Austrian Marshallplan Foundation

Field of study: Mechanical Engineering

University of California, Los Angeles
Laboratory for Laser Spectroscopy and Gas Dynamics

Supervisor:

R. Mitchell Spearrin, PhD, Associate Professor of Mechanical and Aerospace Engineering

Graz University of Technology
Institute of Thermal Engineering

Supervisor:

Univ.-Prof. Dipl-Ing. Dr.techn. Christoph Hochenauer

Graz, October 2024

Affidavit

I declare that I have authored this thesis independently, that I have not used other than the declared sources/resources, and that I have explicitly indicated all material which has been quoted either literally or by content from the sources used.

Date

Signature

Abstract

Premixed and burner-stabilized CH_4 and H_2 flames with O_2 ratios from 21 vol.% up to 100 vol.% were investigated using a Laser absorption spectroscopy (LAS) setup. It was aligned through the center axis of the rotationally symmetric flame of a Flat flame burner (FFB) to infer temperature via lineshape analysis from the absorbance spectra. The targeted species is the CO molecule in a wavenumber range from 2008 cm^{-1} to 2009 cm^{-1}. Since H_2 is a C-free fuel, pure CO was added to the gas mixture in order to use the same LAS setup for all measurements. Therefore, a method to calculate the right amount of additional CO was implemented. Moreover, a 1D-simulation was performed in the computational framework of CANTERA to compare the results with the measured data. During the development of the simulation code, several reaction mechanisms were tested and the results are presented in this work.

As it turned out, the expected theoretical behaviour did not always occur but the underlying reasons responsible for the deviations could be explained. However, the quality of the measured data is decent which is expressed through low uncertainty and an overall good agreement with the simulation in particular close to the burner surface.

Acknowledgments

This research paper is the result of the collaboration between the *Institute of Thermal Engineering* at University of Technology in Graz (TU Graz) and the *Laboratory for Gas Dynamics and Laser Spectroscopy* at University of California, Los Angeles (UCLA). I would like to thank Prof. Christoph Hochenauer and Prof. René Prieler from TU Graz for the great support in the preparation and the postprocessing of my stay abroad. I also would like to thank Prof. R. Mitchell Spearrin from UCLA who made the possibility of a stay abroad during my master's degree possible in the first place. I benefited not only professionally but also personally from the work in his laboratory. After this stay abroad, I have gained a deeper understanding of how politics, economy, society, culture, and research works in the United States of America.

Moreover, I would like to thank DI Stefan Schwarz and DI Georg Daurer from TU Graz for their valuable input during the evaluation of the results. For the great support during the experimental phase, I would like to thank M.S. Nicholas M. Kuenning and M.S. Barathan Jeevarethanam from UCLA.

The project as a whole would not have been possible without sponsors. Therefore, I would like to thank the *Austrian Marshallplan Foundation* and the *Volkswagen AG* who generously supported me financially.

Finally, my deepest gratitude is due to my family, especially my mother Christine and my sister Elisabeth who stood by me and provided me with great social support in all times. This background initially enabled me to study and gave me the courage to go abroad for a longer period of time.

Contents

Acronyms

Symbol	Description
AFT	Adiabatic flame temperature
CARS	Coherent anti-Stokes Raman Scattering
FFB	Flat flame burner
FSR	Free spectral range
HAB	Height above the burner
IR	Infrared
LAS	Laser absorption spectroscopy
LBV	Laminar burning velocity
MFC	Mass flow controller
QCL	Quantum-cascade laser

Nomenclature

Latin symbols

Symbol	Description
A_i	Area under spectra of transition i
c	Propagation speed of photon
D_{ij}	Multicomponent diffusion coefficient species $i - j$
D_i^T	Thermal diffusion coefficient
E_i''	Lower-state energy of species i
E_{lower}	Lower energy state
E_{upper}	Upper energy state
ΔE_{elec}	Electronical energy transition
ΔE_{rot}	Rotational energy transition
ΔE_{tot}	Total internal energy transition
ΔE_{vib}	Vibrational energy transition
H_i	Specific enthalpy of species i
h	Planck's constant
I_0	Incident laser intensity
I_T	Transmitted intensity
I_ν	Spectral intensity
k	Boltzmann's constant
k_ν	Spectral absorption coefficient per unit length
L	Path length
$\dot{M}$	Total mass flow
M_i	Molar mass of species i
n_i	Number density of species i
P_{th}	Thermal power
p	Pressure
$Q(T)$	Boltzmann distribution
R	Gas constant
R_i	Overall production rate of species i
R_{ij}	Area ratio between the two transitions i and j

Symbol	Description
S_{ij}	Linestrength of species i and transition j
T	Temperature
T_0	Reference temperature
$T_{adiabat}$	Adiabate flame temperature
T_v	Spectral transmission
t	time
V_i	Diffusion velocity of species i
V_i	Volume flow rate of species i
v	Flow velocity
v_{exit}	Initial exit flow velocity
v_L	Laminar burning velocity
Δv_c	Collisional width
Δv_D	Doppler width
X_i	Concentration of species i
Y_i	Mass fraction of species i

Greek symbols

Symbol	Description
α_ν	Spectral absorbance at frequency ν
λ_i	Thermal conductivity coefficient of species i
ν	Wave number/Frequency
$\nu_{0,i}$	Line position/Center frequency of species i
ρ	Density
Φ	Equivalence ratio
Φ_{ij}	Lineshape of species i and transition j

1 Introduction

In times of global warming, the reduction of greenhouse gas emissions, especially carbon dioxide, is one of the key drivers in research projects all around the world. Many branches of our modern lives are facing radical changes. Especially the Russian war in the Ukraine accelerated the transformation to renewable ressources because the years of cheap energy in the form of natural gas are over [1]. In particular, energy-intensive companies are at the mercy of this trend as they cannot simply convert their natural gas-powered processes to produce industrial heat. Moreover, changes in production processes are always accompanied by very high investments. For these reasons, the transformation in this branch is very challenging.

Two approaches to reduce the carbon dioxide emissions in industrial heating applications are the use of H_2 as a fuel and higher O_2 ratios to increase the overall efficieny. These aspects are further investigated in this paper from a scientific perspective.

The laboratory-scale FFB which can be seen in figure 1.1 serves as a plattform for the fundamental experiments. This burner type is characterized by a premixed, laminar, homogeneous and rotationally symmetric flame. During the test series of this work, the ratio of O_2 was increased from 21 vol.% (air conditions) up to 100 vol.% (pure O_2). CH_4 and H_2 were used as fuels. The thermodynamic state variable temperature T was chosen as the parameter to investigate and compare the changes in the flame. Measuring temperature in this sensitive environment is not trivial and needs a method which is not affecting the flame itself. Therefore laser diagnostic methods are very well qualified because they are not only an in-situ and non-intrusive but also quantitative measurement technology.

For this paper specifically, LAS has been choosen because it is a precise and well experienced method in the field of temperature measurement in flames and gases [2]. The LAS alignment is presented in figure 1.2. As the energy spectrum of *CO* provides a suitable linepair at wave numbers between 2008 and 2009 cm^{-1}, it is the targeted species for this work. Theoretical analyses of the absorbance spectra, validated by preliminary experiments, showed that there will be probably not enough *CO* in some operating states. Past investigations solved this issue by seeding-in pure *CO* directly into the fuel-oxidizer-mixture. They suggested a small effect on the reaction mechanisms in the flame [3]. For this reason, the same method is applied in this work to enrich the species concentration of *CO* to get an adequate absorbance factor but also presenting the calculation procedure behind it.

Both literature and simulation were used to validate the experimental results of the present work. A simulation code written in the CANTERA environment provides a solid 1D-approach to investigate the species and temperatures numerically. The reaction mechanisms *Aramco 2.0, FFCM 2.0, GRI 3.0, GRI 3.0 highT, Hashemi, San Diego mech, Smooke* were implemented, compared to the experimental data of this work and the most suitable one was selected. Furthermore, the simulation allows to estimate the influence of seeding-in pure *CO* into this particular flame

configuration. This is specifically important for the H_2 flame, as its temperature could not be measured with the same laser setup without the additional CO.

All results are summarized and dicussed at the end of this paper. Part of this final chapter is also an outlook which provides ideas for further research areas.

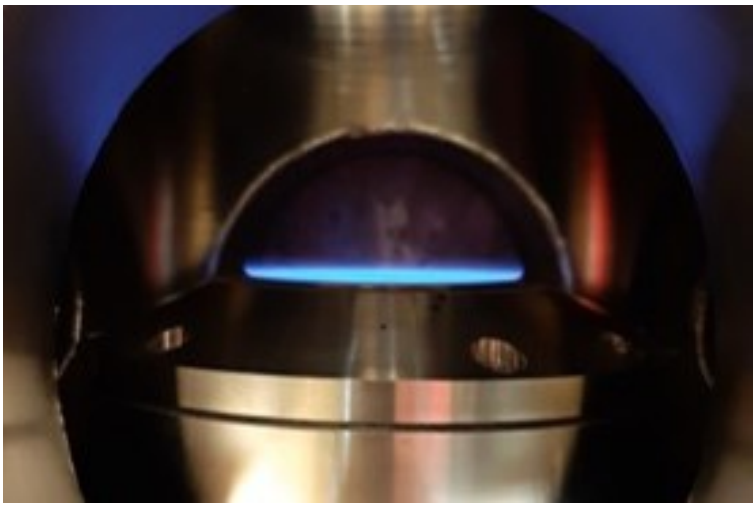

Figure 1.1: Laminar and premixed flat flame (CH_4 with 21 vol.% O_2) above the surface of the FFB.

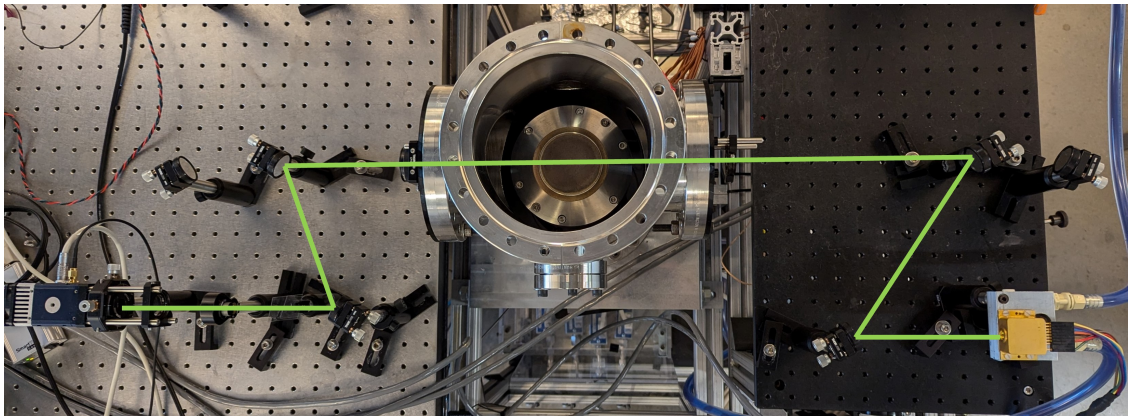

Figure 1.2: Experimental setup showing the FFB in the center and the LAS alignment for measuring CO with the laser on the right and the detector on the left side.

2 1D-Simulation

In order to be able to estimate the test conditions, a simulation code written for this work was executed in the CANTERA framework in advance. Figure 2.1 shows a simple schematic of the FFB and its intial simulation conditions that needed to be predefined. As the result (outlet conditions), CANTERA provides a 1D-profile for species and temperature along the vertical z-axis above the burner surface.

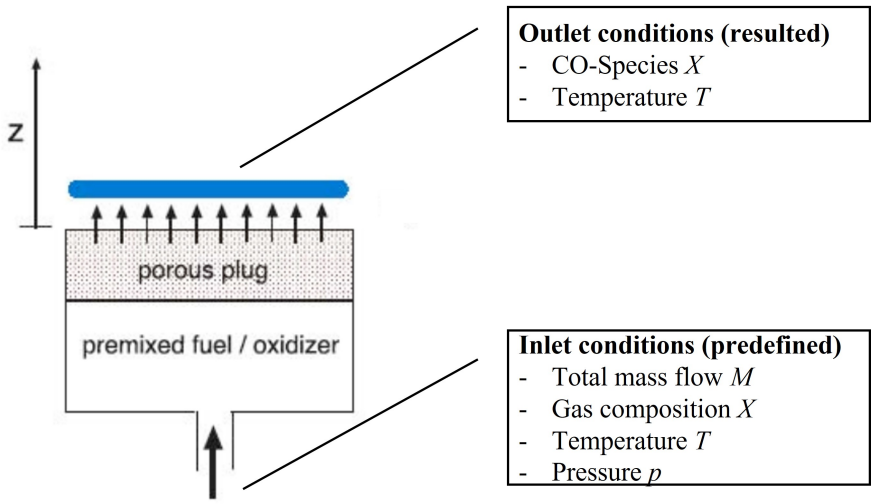

Figure 2.1: Schematic of the FFB and the initial simulation conditions.

CANTERA offers several classes for various test conditions. The class *BurnerFlame* was developed for a *burner-stabilized and premixed fuel/oxidizer mixture* which fits best the FFB and is therefore used in this work [4]. The porous plug in the schematic is part of the real burner but not important for the simulation which assumes a perfectly premixed fuel-oxidizer-mixture. The combustion reaction begins slightly above the burner surface in the blue area and a specific mechanism must be set in order to control the reaction kinetics. Several reaction mechanisms were applied in this work.

In order to obtain a determined solution, the conditions seen in figure 2.1 must be initially set. The total mass flow M will change during the test series as a result of the varied composition X which contains the fuel and oxidizer ratios. The inlet temperature T and pressure p are specified with normal conditions ($293.15\ K$, $1\ atm$). Both values remain constant throughout this work.

CANTERA provides a *damped Newton solver* with internal time integration to approximate the analytical solution. The numerical solution process is terminated when the residual of the solver is smaller than the tolerances specified by the user. All general conservation equations are calculated for perfect gas. Moreover the energy equation must be solved because initially no temperature data

is available. The Soret effect is enabled while the radiative heat transfer mechanism is disabled. The simulation code uses the multi-phase transport model [4].

The conservation equations calculated by CANTERA are presented more detailed in chapter 3.2.1.

2.1 Reaction mechanisms

As described above, various reaction mechanisms for CH_4-H_2-combustion were implemented. During the selection of pure hydrogen mechanisms, many of them were rejected because they did not incorporate *CO* reaction kinetics. However, this was a precondition for using the same LAS setup throughout this work. To begin with, some important information is listed in table 2.1. *Aramco 2.0, FFCM 2.0, GRI 3.0* and *San Diego mech* are mechanisms that can be both used for CH_4 and H_2. *Hashemi* and *Smooke* are primarily designed for CH_4 combustion. *Smooke* is the only reduced mechanism which is derived from *GRI 3.0*. All other mechanisms have a large number of species and reactions meaning that they are developed very detailed.

Table 2.1: Characteristics of the reaction mechanisms tested in the simulation code of this work.

Reaction mechanism	**Year**	**Species**	**Reactions**
Aramco 2.0 [5]	2016	493	2716
FFCM 2.0 [6]	2023	96	1054
GRI 3.0 [7]	2000	53	325
Hashemi [8]	2016	68	631
San Diego mech [9]	2016	57	268
Smooke [10]	1991	16	25

The reaction mechanisms were investigated using two exemplary combustion cases. A 1 kW CH_4 *air* combustion (21 vol.% O_2) was the first case because air is the most widespread oxidizer and with CH_4 as the fuel, it combines all species that are relevant for the combustion reactions: *C*, *H*, *O* and *N*. It is important to mention that pure CO was also added in this combustion scenario in order to increase the absorbance of *CO* to a solid level. More information on seeding-in *CO* can be found in chapter 3.4. In figure 2.2 (a), the temperature data from the FFB experiment along the vertical axis is plotted against the simulation data. All reaction mechanisms show similar behaviour and fluctuate in a range of approx. 50 K but overestimate the experimental temperature. When comparing the *CO*-concentration data in figure 2.2 (b), the consistency with the *Hashemi* mechanism is noticeable, in particular, up to 5 mm Height above the burner (HAB). In higher ranges above the burner the deviation increases because all simulated mechanisms predict constant values but the experimental *CO* concentration decreases. In general, the simulaton data differs among each other by approx. 0.3 vol.%.

The second case is a 1 kW H_2 air combustion (21 vol.% O_2) which can be seen in figure 2.3. Since this is a *C*-free combustion reaction, it was necessary to add *CO*. The agreement between simulated and experimental temperature data strongly depends on the reaction mechanism but

is in general better than for the first combustion case. *Aramco 2.0* hits the temperature very well, especially up to *5 mm*. Among the mechanisms, the absolute deviation between the extreme values is approx. 50 K. Figure 2.3 (b) shows the *CO* concentration for the H_2 flame. All simulations are close together (~ 0.3 vol.%) but overestimate the experimental *CO* concentration data. The deviation is almost 1 vol.% and it seems like that the mechanisms expect *CO* to interact less with the combustion meaning the *CO* concentration remains constantly. However, the experimental *CO* decreases almost linearly.

In order to find a compromise for a decent mechanism, the temperature diagrams are in the foreground, the *CO* concentration is just a supportive argument because through LAS both variables are measured independently. This means that the agreements of temperature and species concentration between experiment and simulation are also independent. More information on this behaviour can be found in chapter 3.3.4. The first combustion case suggests *GRI 3.0* or *Aramco 2.0* for temperature and *Hashemi* or *FFCM 2.0* for *CO* species concentration. For the second case, *Aramco 2.0* seems to be a good choice for temperature. As described above, the simulated *CO* concentration data for the H_2 flame is not be taken into account because none of the mechanisms seems to be able to model the reaction kinetics in a suitable way. Computational time is another important criterium. From this perspective, *Aramco 2.0* is not adequate because the computational time on the available computers is much longer and not justifiable for the small improvement. This was to be expected when looking into table 2.1 again showing the level of detail based on species and reactions. All other mechanisms could be solved fast enough.

Overall however, *FFCM 2.0* is the best compromise and therefore selected as the reaction mechanism for this work. It shows solid agreement when comparing to the temperature (both combustion cases) and concentration (first combustion case) data in particular in the important area close to the burner surface ¡5 mm HAB.

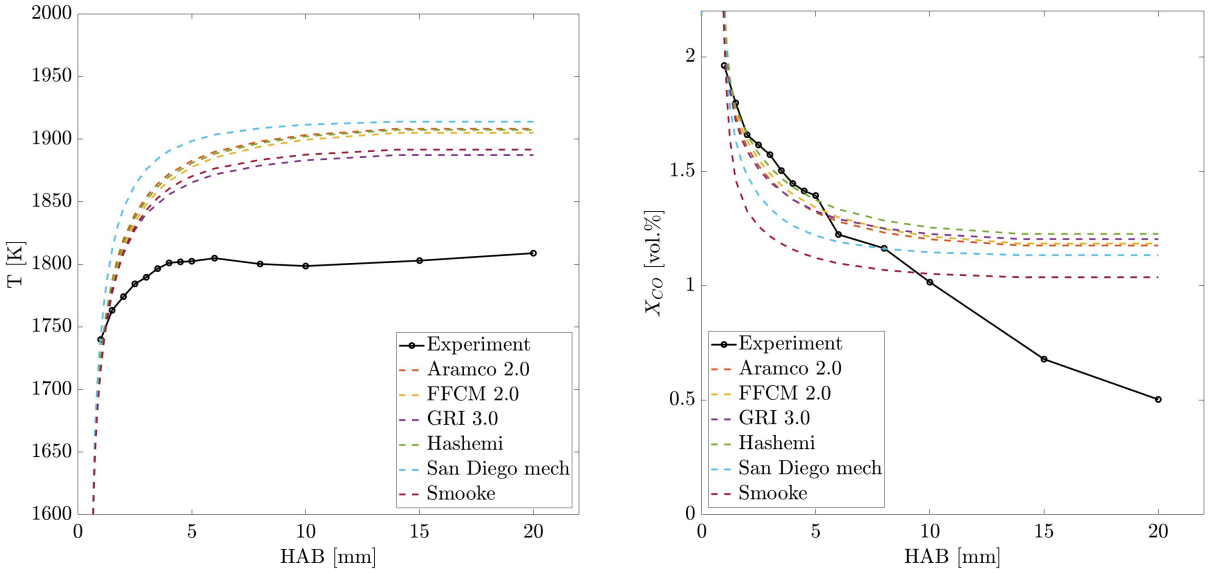

(a) (b)

Figure 2.2: (a) Experimental temperature data from a 1 kW CH_4 air flame (21 vol.% O_2) compared with various reaction mechanisms, (b) Experimental concentration data from a 1 kW CH_4 air flame (21 vol.% O_2) compared with various reaction mechanisms.

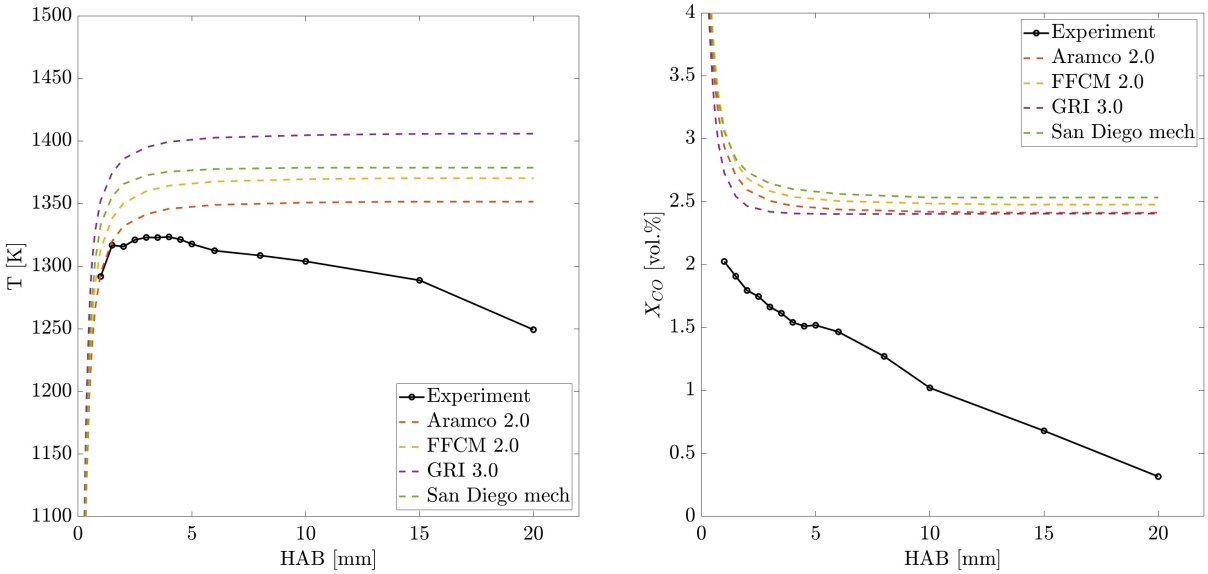

(a) (b)

Figure 2.3: (a) Experimental temperature data from a 1 kW H_2 air flame (21 vol.% O_2) compared with various reaction mechanisms, (b) Experimental concentration data from a 1 kW H_2 air flame (21 vol.% O_2) compared with various reaction mechanisms.

3 Theoretical principles

In this chapter, the underlying theoretical principles used in this work are presented. The focus lies on the FFB, its characteristic flame, the methodologies of LAS and finally explanations on the addition of pure *CO*.

3.1 Premixed flat flame

The FFB, also known as *McKenna Burner* in the literature, provides the premixed flat flame which is investigated in this work. Figure 3.1 (a) shows a schematic of the burner. Following the path of the fuel gas, it starts with the inlet where the fuel and oxidizer enter the mixing chamber. Above that, the porous plug which is made from sintered bronze (excellent heat conduction characteristics) acts as a porous barrier for the gas and a stabilizer for the flame. This is done by mitigating any pressure surges, calming, distributing and homogenization of the gas components. Moreover the channels through the plug are narrow enough that there is no propagation of the flame through them due to excess heat loss. This ensures that flashback is prohibited. The radiative heat transfer from the flame to the porous plug requires cooling. This is operated by an Archimedian spiral cooling circuit with water at room temperature which also minimizes radial temperature gradients. Coaxial around the mixing chamber so called shroud gas can enter the shroud gas chamber. Above that a similar porous plug is mounted. It ensures an even distribution along the circumference. Ideally the shroud gas creates an inert athmosphere for the flat flame so that the environment has a negligible effect. Typical gases are N_2 or Ar.

Regarding the flame, the FFB yields conditions that are higly repeatable and ideally only change along the vertical flame axis. Because of the 1D-character, the burner is a perfect calibration source for combustion research [13]. Figure 3.1 (b) shows the change of the two variables temperature and concentration along the vertical axis above the burner surface. As the flame has a laminar nature up to 10 - 15 mm HAB depending on the conditions, the curves in the diagram are stationary in time.

The reaction zone is the region where most of the chemical processes occur resulting in a typically thin and well-defined flame front (see also figure 1.1). Fuel and oxidizer are coming from the preheat zone and react to combustion products. This leads to a steep gradient in the species concentration and a rapid temperature increase due to the exothermic character. Furthermore, this region is populated by many intermediate species because combustion is generally a multi-step process.

Two very important variables in the context of flame stabilization are the exit velocity v_{exit} of the unburned gas leaving the porous plug and the free-flame Laminar burning velocity (LBV) v_L. Three different cases, shown in table 3.1, can be distinguished. Case 1 will eventually end with

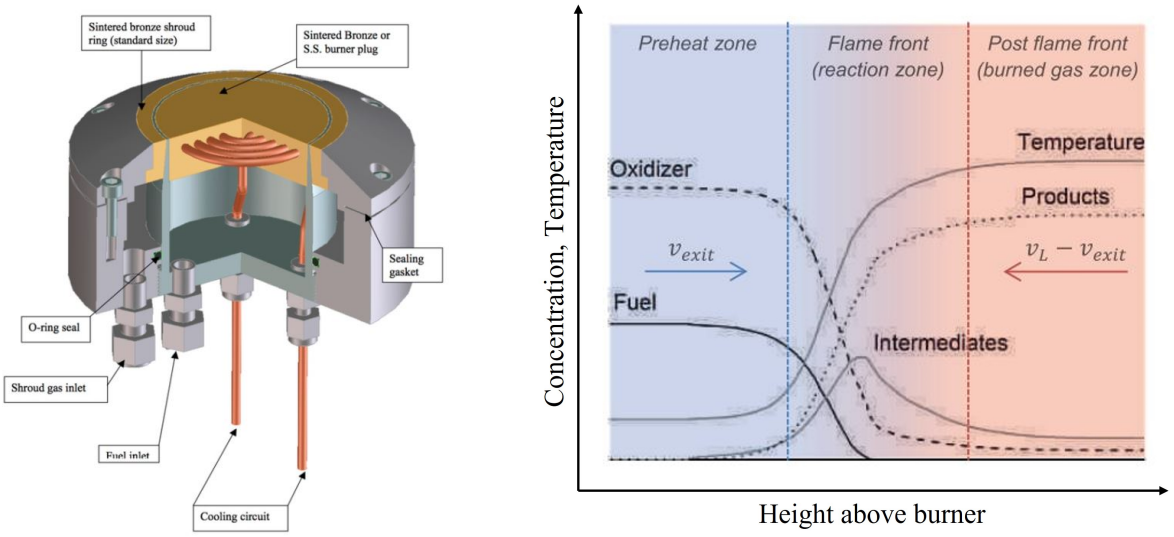

(a) (b)

Figure 3.1: (a) Schematic of the FFB used in this work [11], (b) Exemplary reaction schematic of a 1-D premixed flame, adapted from [12].

the flame extinguishing and case 2 with a stationary and stable flame. However, case 3 is the desired one with an upstream driven flame front. A flashback is likely to happen and will end in an explosion in the worst scenario when the flame is propagating back into the supply lines, except from the specific burner deck of a FFB. As described further up, the narrow channels of the porous plug prohibit the flame propagating upstream and minimize the risk of a flashback. As this specific type of burner ensures that the flame remains above the plug, the flames are so called burner-stabilized. Indeed, the upstream driven environment is responsible for transferring heat through conduction from the flame to the burner. This principle can be used to control the flame temperature but was not used in this work as other goals have been pursued [12].

Table 3.1: Relation between v_{exit} and v_L and the resulting effects on the flame stabilization on the FFB [12].

	Flame front	**Flame on the FFB**
Case 1: $v_{exit} > v_L$	downstream driven	blow-off
Case 2: $v_{exit} = v_L$	stationary	stable
Case 3: $v_{exit} < v_L$	upstream driven	no flashback/**stabilized**

3.2 Calculating 1D flat flame structures

3.2.1 Governing conservation equations

Assuming the premixed flat flame of the FFB to be 1-D is the fundamental precondition for the following calculation. It is based on the conservation equations of mass, gas phase species and

energy. At constant pressure while neglecting the effects of viscosity, radiation and external forces, the steady flame can be described with the following governing equations [14, 15].

Conservation of total mass:

$$\frac{d}{dz}(\rho v) = \frac{d}{dz}(\dot{M}) = 0 \tag{3.1}$$

Conservation of species mass:

$$\frac{d}{dz}\left[Y_i \rho (v + V_i)\right] = R_i \tag{3.2}$$

where the diffusion velocity V_i is:

$$V_i = \frac{1}{\rho_i}\left(\frac{c^2}{\rho} M_i \sum_j M_j D_{ij} \frac{\partial X_j}{\partial x} - \frac{D_i^T}{T}\frac{\partial T}{\partial x}\right) \tag{3.3}$$

Conservation of energy:

$$\frac{d}{dz}\left[\sum_i Y_i \rho H_i (v + V_i) - \lambda \frac{dT}{dz}\right] = 0 \tag{3.4}$$

where the thermal conductivity coefficient λ is:

$$\lambda = \frac{1}{2}\left[\sum_i x_i \lambda_i + \left(\sum_i \frac{x_i}{\lambda_i}\right)^{-1}\right] = 0 \tag{3.5}$$

Ideal gas equation of state:

$$p = \rho R T \sum_i \frac{Y_i}{M_i} = 0 \tag{3.6}$$

The conservation of total mass in equation 3.1 states that the total mass flux $\dot{M}$ is independent of the vertical axis z. This is a result of the assumption that the total amount of mass is not affected by any chemical reactions above the burner surface. In equation 3.1, ρ is the total mass density, and v the mean mass flow velocity.

Equation 3.2 is the conservation of species mass where the species mass fraction itself is named Y_i. The source term R_i on the right side is the production rate of the mass fractions of indiviual species i. This means that Y_i can indeed change in time due to chemical reactions while the total mass flux $\dot{M}$ is constant. However, the $\sum R_i$ which is the overall production rate considering all individual species must be zero because chemical reactions can neither form nor destroy mass. The last unknown component stated in equation 3.3 is the diffusion velocity V_i which is relative to the mean mass flow velocity. It results from the species concentration gradient (Fickian diffusion) and the thermal gradient (Soret effect). Each species i has its own V_i consisting of the mass density ρ_i, the molar mass M_i, the multicomponent diffusion coefficients D_{ij}, the species mole fraction X_i and the thermal diffusion coefficient D_i^T. x is here the radial axis of the FFB.

Combustion usually consists of exothermic chemical reactions which cause a heat release and leads to a steep temperature gradient. Therefore the conservation equation of energy stated in 3.4 must also be taken into account. H_i is the specific enthalpy of species i, and λ the thermal conductivity coefficient of the mixture. The first term quantifies the change in enthalpy resulting from the flow of species and the second term quantifies the heat flux which comes from the transport of energy

due to the temperature gradient. Equation 3.5 is an empirical law for gas mixtures which can be used with reasonable accuracy for calculating λ from the thermal conductivities of the individual components λ_i [12, 16].

The ideal gas equation of state, also known as ideal gas law, adjusted to gas mixtures in equation 3.6 completes the system of equations. R is the gas constant.

All conservation equations now build up a system of $(z+2)$ linearly independent equations with z standing for the number of species in the flame. The system is sufficient to solve because V_i can be calculated from the known variables at the inlet temperature and species concentration [17]. Finally, the unknown variables at the outlet T, ρ, v and $(z-1)$ independent parameters from the set Y_i can be calculated.

All previous considerations assume that the boundary conditions are choosen appropriate. For burner-stabilized premixed flat flames, the total mass flux $\dot{M}$ is fixed. At the inlet boundary, temperature and species concentration must be specified while vanishing gradients are defined at the outlet boundary [12].

These fundamentals for calculating flat flames form the basis for chapter 2 in which the 1D-simulation in CANTERA is explained in an applied context.

3.3 Spectroscopic methodologies

LAS was selected as the optical measurement technology for this work for several reasons. First, very hot gases like flames can be measured due to the high intensities of the laser. They come from the high collimation of the light which is another aspect, allowing the light to travel distances magnitudes longer than needed in this work. And last, the lasers used in LAS are often spectrally narrow and tuneable in wavelength. This leads to high accuracy for quantitative measurements of absorption spectra which enables the derivation of species concentration and temperature. As an introduction, figure 3.2 shows a simple exemplary schematic of the core setup.

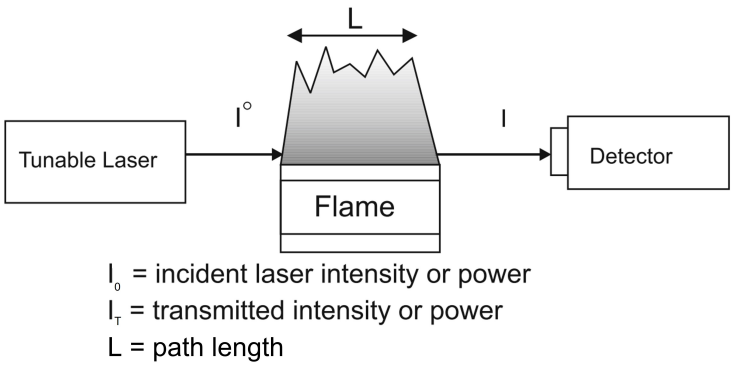

Figure 3.2: Experimental LAS schematic, adpated from [18].

The theory of LAS is extensively outlined in literature but to clarify fundamendals and nomenclature briefly discussed here [18].

First, there are four separate possibilities when collimated light at frequency ν enters a gas or flame, illustrated by formula 3.7.

$$1 = \underbrace{\text{absorption}}_{\alpha_\nu} + \underbrace{\text{reflection}}_{=0} + \underbrace{\text{scattering}}_{=0} + \underbrace{\text{transmission}}_{T_\nu} = \alpha_\nu + T_v \tag{3.7}$$

All probabilities sum up to 1 and in the common case reflection and scattering are negligible while the conservation of energy applies being responsible for the result $1 = \alpha_\nu + T_\nu$. Transmission T_ν and even more absorption α_ν are *the* relevant quantities for applying LAS in order to measure thermodynamic properties of a gas/flame *quantitatively*.

3.3.1 Absorption

Absorption is by definition the quantum state change from a lower to a higher energy of an atom or a molecule by absorbing a photon [18]. This means each quantum energy state has a discrete amount of energy and angular momentum. Hence, molecular energy is quantized. The absorbed energy can be stored in three modes, illustrated by equation 3.8.

$$\Delta E_{tot} = \underbrace{\Delta E_{rot}}_{\text{rotation}} + \underbrace{\Delta E_{vib}}_{\text{vibration}} + \underbrace{\Delta E_{elec}}_{\text{electronic}} \tag{3.8}$$

Summed up, these modes are the total internal energy E_{tot} of an atom or a molecule. Note again that the transitions between energy states are discrete meaning that just light with a specific frequeny/wavelength is able to transfer the energy. This is where Planck's law (equation 3.9) comes into play. It connects the molecular transition (emission and absorption) between two quantum states with the frequency ν of the corresponding electromagnetic wave. h is Planck's constant.

$$\Delta E = \Delta E_{rot} + \Delta E_{vib} + \Delta E_{elec} = E_{upper} - E_{lower} = h\nu \tag{3.9}$$

Figure 3.3 gives an idea which transition is triggered at which frequency. In this work, the red marked range around a wavelength of 5 μm is of interest to meet discrete energy states of CO. This means that the wavelength of the laser must be in the Infrared (IR).

Moreover, figure 3.3 shows moreover that electronic transitions need the highest amount of energy (UV/visible range), followed by vibrational (IR range) and at least rotational (microwave range) transitions. In general, electronic transitions are accompanied by changes in vibrational and rotational energy, so called rovibronic transitions. While vibrational transitions are accompanied by rotational, so called rovibronic transitions. Just rotational transitions occur allone due to their low energy.

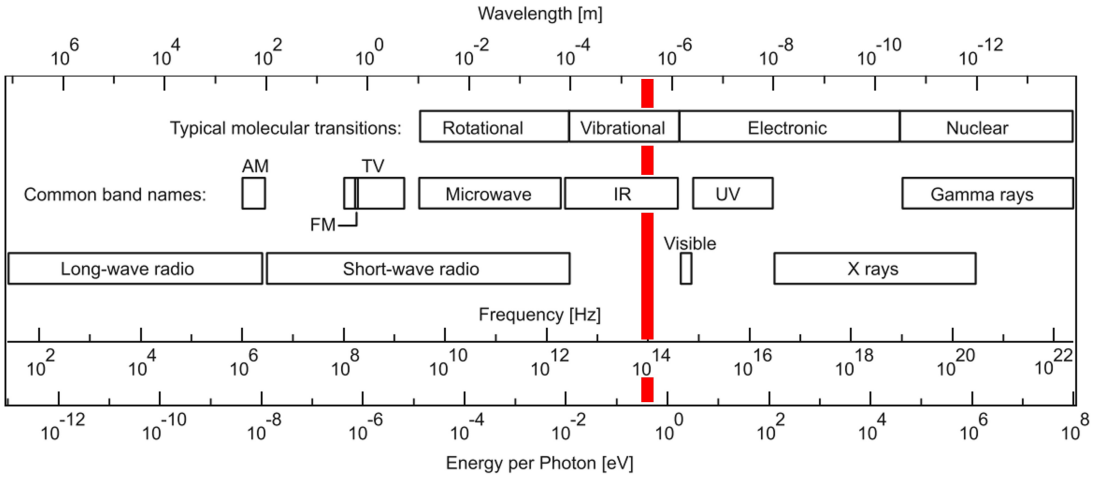

Figure 3.3: Electromagnetic spectra with the red marked range of interest in the IR, adpated from [18].

3.3.2 Beer-Lambert law

In the following, the derivation of the Beer-Lambert law is outlined, starting with α_ν which is taken from equation 3.7 and further processed [18].

$$\alpha_\nu \equiv \frac{-dI_\nu}{I_\nu} = k_\nu dx \tag{3.10}$$

$$\int_I \frac{-dI_\nu}{I_\nu} = \int_x k_\nu dx \tag{3.11}$$

Beer-Lambert law:

$$\alpha_\nu = -ln\left(\frac{I_t}{I_0}\right)_\nu = k_\upsilon L \tag{3.12}$$

The spectral absorbance α_ν is the fraction of incident light I_ν that is absorbed for the frequency range $\nu \to \nu + d\nu$. It can also be expressed as k_ν, the spectral absorption coefficient per unit length, see equation 3.10. Equation 3.11 shows the application of the integral over the path length L of the gas/flame domain (see figure 3.2). The result of the integration using the boundaries $x = [0, L]$ and $I = [I(x = 0) = I_0, I(x = L) = I_t]$ is stated in equation 3.12. This expression is also called the Beer-Lambert law which may be *the most important relation in absorption spectroscopy* [18]. The relation I_t/I_0 is the fractional transmission at frequency ν consisting of experimentally measured transmitted intensity I_t and incident laser intensity I_0. The term $k_\nu L$ shows that the absorbed intensity is proportional to the spectral absorption coefficient and the path length of the domain.

The Beer-Lambert law is not only the fraction of absorbed intensity but also relates the measured absorbance spectra to thermophysical properties of a flow showed in equation 3.13. It consists of the number density of species i, n_i [cm^{-3}], temperature T [K], and pressure P [atm], as well as the path length L [cm] [19].

$$\alpha_{ij}(\nu) = -\ln\left(\frac{I_t}{I_0}\right)_\nu = n_i x_Y P L S_{ij}(T)\phi_{ij}(\nu, P, T, X_Y) \tag{3.13}$$

S_{ij} [cm^{-1}/molecule cm^{-2}] is the so called line strength and ϕ_{ij} [cm^{-1}] the so called lineshape. Both contain temperature and pressure dependence and are described more detailed in the next chapter.

3.3.3 Basic elements of spectroscopy

First, all elements of spectroscopy are based on so called *lines*. A line is the term for an energy transition from one quantum state to another. It can be illustrated as a line in a molecular spectra. Figure 3.4(a) shows the *CO*-lines targeted in this work.

The basic elements of spectroscopy are line strength and lineshape as well as line position. A line position is the part of a spectrum illustrating a transition from one quantum state to another, e.g. rotational line in a spectrum correponds to a change in a molecule's rotational energy.

The lineshape function ϕ_{ij} characterizes the relative variation in the spectral absorption coefficient with frequency. Broadening mechanisms (see table 3.2) in the medium are responsible for this variation. This variable is of interest because it allows to determine properties of the medium such as temperature, pressure, and velocity.

Table 3.2: Explanation of different broadening mechanisms which influence the lineshape function [18].

Broadening mechanism	**Explanation**
Natural broadening	Spontaneous emission without interaction with other atoms.
Collisional Broadening (Pressure broadening)	Collisions with other atoms/molecules
Doppler broadening	Molecule with velocity component in the same direction as the propagation of a beam of light causing a shift in the frequency followed by absorbing a photon
Stark broadening	Coulomb forces can perturb the energy levels causing significant broadening
Instrument broadening	Insuffiecient resolution, power broadening, transit-time broadening

The last basic element of spectroscopy is the line strength S_{ij}, also known as "integrated absorption". This quantity provides a relative strength for a particular transition from one to another energy state in a molecular band and thereby influences the shape of a spectrum [20]. It is independent of the line shape thus independent from broadening mechanisms and in our case simply a function of T. Through this, it is possible to derive temperature and therefore selected in this work. A line strength diagam for *CO* can be found in figure 3.4.

The equation of temperature-dependent line strength is shown in 3.14. It can be calculated from the molecule's reference temperature line strength $S_i(T_0)$, the absorbing molecule's partition function $Q(T)$, also known as Boltzmann distribution, the lower-state energy of the transition E_i'', and the center frequency of the transition $\nu_{0,i}$. All these quantities are documented in databases.

Just a short addition to the Boltzmann distribution $Q(T)$: It determines the fraction of molecules in a particular energy state i.

$$S_i(T) = S_i(T_0)\frac{Q(T_0)}{Q(T)}\left(\frac{T_0}{T}\right)\exp\left[\frac{-hcE_i''}{k}\left(\frac{1}{T}-\frac{1}{T_0}\right)\right] \times\left[1-\exp\left(\frac{-hc\nu_0,i}{kT}\right)\right]\left[1-\exp\left(\frac{-hc\nu_0,i}{kT_0}\right)\right]^{-1} \tag{3.14}$$

There are just two unknowns left in equation 3.14 which are the actual line strength $S_i(T)$ and the associated temperature T. To solve this problem in order to obtain the temperature of a measured medium, it is necesary to include another relation. This can be inferred from the absorbance spectra using quantitative lineshape measurements which will be introduced in the next chapter.

3.3.4 Quantitative lineshape measurements

The species concentration, pressure, temperature, and flow velocity can be determined quantitatively from the size and shape of different transitions.

The area under the absorption transition is a possibility to calculate species concentration and pressure which is stated in the following equations. Initial point is the Beer-Lambert law from equation 3.12 giving the opportunity to get the absorbance from the attenuated intensity of the laser light divided by the original intensity.

$$A_i = \int_{-\infty}^{+\infty} \alpha_\nu(\nu)\, d\nu \tag{3.15}$$

$$A_i = S_i P X_j L \tag{3.16}$$

$$X_j = \frac{A_i}{S_i P L} \tag{3.17}$$

The integration of the absorbance over the frequency in equation 3.15 results in the area A_i under the spectra. Equation 3.16 gives the correlation between the area and the variables of interest. This formula resembles equation 3.13 but the integral causes the normalized contribution of the line shape to disappear. The last equation 3.17 can be used exactly as specified here because all quantities are known except the species concentration X_j. If the species concentration is known, this expression can obviously be transformed to get pressure.

The quantity temperature can be measured with two different lineshape techniques. The first is suitable in Doppler-limited applications, where the pressure broadening is negligible. This does not apply for the flame of the FFB.

Therefore the second method, the so called *two line* technique, is used in this work because it is particularly suitable in pressure broadend regimes. Previously in equation 3.14, the temperature dependency of the line strength was demonstrated. If now the integrated absorbance area of a transition is taken from equation 3.16 and applied for two lines, the ratio of these two areas leads

to the disappearance of pressure, species concentration and path length. Only temperature and lower-state energy for the respective transition remain. Lower-state energy is typically known from tabulations thus temperature can be inferred. The achievement of this mathematical operation needs to be emphasized again. It is now possible to measure temperature without the knowledge of pressure, species concentration or path length meaning all these quantities have no influence on the temperature anymore. The associated equations are presentend in 3.18 and 3.19

$$R_{12} = \frac{A_1}{A_2} = \frac{S(T,\nu_1)}{S(T,\nu_2)} = \frac{S(T_0,\nu_1)}{S(T_0,\nu_2)} \exp\left[-\left(\frac{hc}{k}\right)\left(E_1'' - E_2''\right)\left(\frac{1}{T} - \frac{1}{T_0}\right)\right] \tag{3.18}$$

$$T = \frac{\frac{hc}{k}\left(E_2'' - E_1''\right)}{\ln R_{12} + \ln\frac{S_2(T_0)}{S_1(T_0)} + \frac{hc}{k}\frac{(E_2' - E_1')}{T_0}} \tag{3.19}$$

where $S(T_0,\nu_1)$ and $S(T_0,\nu_2)$ are the strengths of the two lines at the reference temperature T_0, ν_1 and ν_2 are the linecenter frequencies and E_1'' and E_2'' are the lower-state energies for the two transitions. Induced emission terms have been neglected [18].

All previous lineshape measurement techniques are explained in a more applied way in the next chapter 3.3.5. There are also other possibibilities to infer the presented quantities. For example, in a collisionally dominated regime with the knowledge of the collisional width $\Delta\nu_c$ and Doppler width $\Delta\nu_D$ the change in linewidth is linearly dependent on pressure, with an additional dependence on temperature and gas composition. This method is not used in this work but more information can be found in [19].

3.3.5 Wavelength selection

CO was selected as the targeted species. Since *CO* is ubiquitous in hydrocarbon combustion as a stable intermediate/product it is perfectly suitable for CH_4 combustion. Obviously it is not the best choice for H_2 combustion because the chemical reactions are *C*-free. The workaround for H_2 is to add pure *CO* into the flame which is explained in detail in chapter 3.4.

Furthermore, there are spectroscopic aspects making *CO* a good choice: (i) It is one of the strongest absorbers in the IR enabling higly sensitive temperature measurement, (ii) *CO* provides well separated lines due to its simple diatomic structure and singlet electronic ground state permitting accurate fitting to spectral parameters, (iii) compared to other common species in combustion gas (e.g. H_2O) *CO*'s broadening coefficients remain almost constant even in environments with changing temperature, pressure etc. reducing the uncertainty in the spectroscopic broadening parameters [3].

Specifically, the following two lines from the rovibrational band of *CO* near 5 μm ($\nu_0 \sim 2008.5\,\mathrm{cm}^{-1}$) were selected: P(2,20) and P(0,31). P(3,14) must also be considered because it will influence P(0,31) in its spectral lineshape. These lines can be seen in figure 3.4(a) with frequency ν on the x-axis and linestrength S_{ij} on the y-axis. The large difference between the line strengths S_{ij} of P(2,20) and P(0,31) is noticeable enhancing sensitivity which is desirable for the two-line thermometry used in this work. Figure 3.5 shows this sensitivity in respect to temperature and it is remarkable how both transitions react. The Boltzmann distribution determines the population of the energy

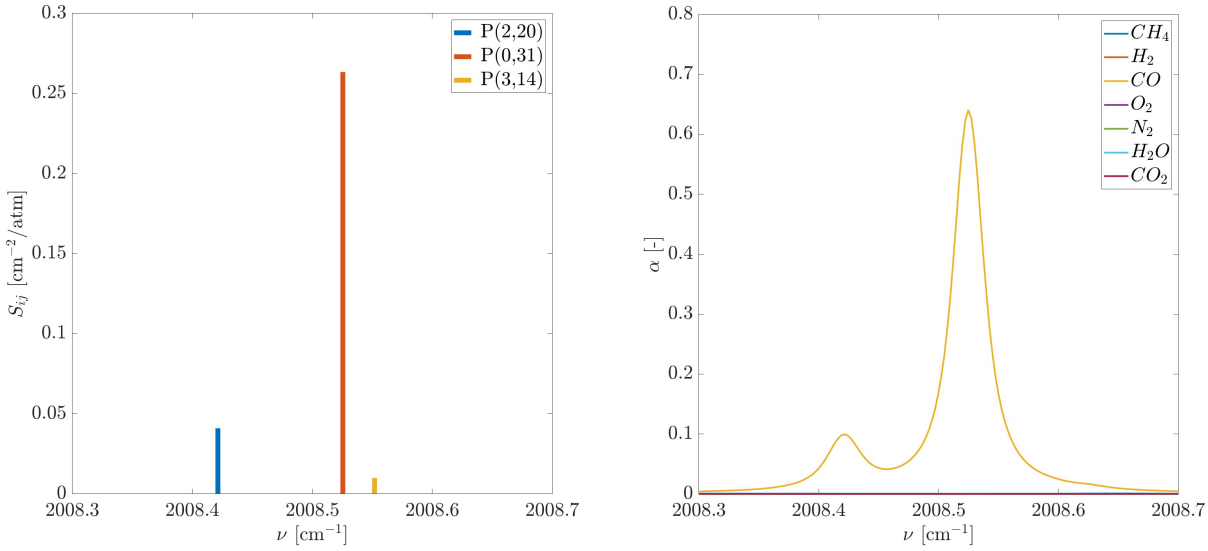

Figure 3.4: (a) Suitable lines from the spectra of *CO* to measure temperature in the FFB flame, from HITRAN database [21, 22] (b) Comparison between the absorbance of all relevant molecules under representative conditions, from HITRAN database [21, 22].

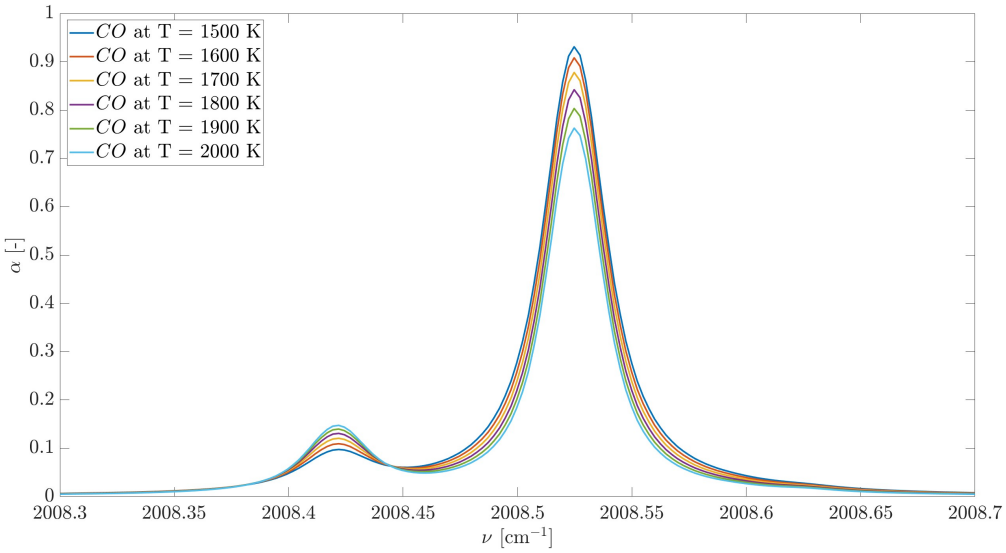

Figure 3.5: Absorbance spectra of *CO* with a focus on how the Boltzmann distribution changes for different temperatures [22].

states: For higher temperatures the left peak P(2,20) rises in population resulting in a larger area and the right peak P(0,31) sinks in poulation leading to a smaller area. But there are limits which must be considered. Figure 3.4(b) shows the absorbance of each transition: The blue line in 3.4(a) corresponds to the left peak of the yellow *CO* curve while the orange line corresponds to the right peak. The limit here concerns the absorbance itself: A rule of thumb is $0.1 < \alpha < 2.3$. Values below 0.1 describe an optically thin regime, values above 2.3 an optically thick regime, both cases should be avoided in spectroscopy [18]. Moreover, an absorbance of $\alpha \approx 1$ provides the highest signal-to-noise ratio [23]. The two rules from practice are considered for all experiments carried out in this work. In addition, figure 3.4 (b) reveals the spectral isolation of the *CO* line

pair compared to all other combustion species that could occur making the measurement less susceptible to disturbances. And a last aspect is the close spacing of the two lines making them accessible for a single narrowband laser.

Finally, a look at the literature reveals that previous works [2, 3, 19, 24] have already dealt with this line pair of *CO*. They have shown an excellent agreement with theoretical calculations thus being very reasonable for the application in quantitative measurements.

3.3.6 Data processing and fitting procedures

The data processing forms the basis for the analysis of the measured absorbance spectra enabling to extract thermodynamic quantities. Figure 3.6 shows the complete procedure starting with the data acquisition with the *Picoscope* continuing with the data processing via MATLAB and finally the solved absorbance in the red box. The individual steps generally follow the mathematical considerations of the previous chapters.

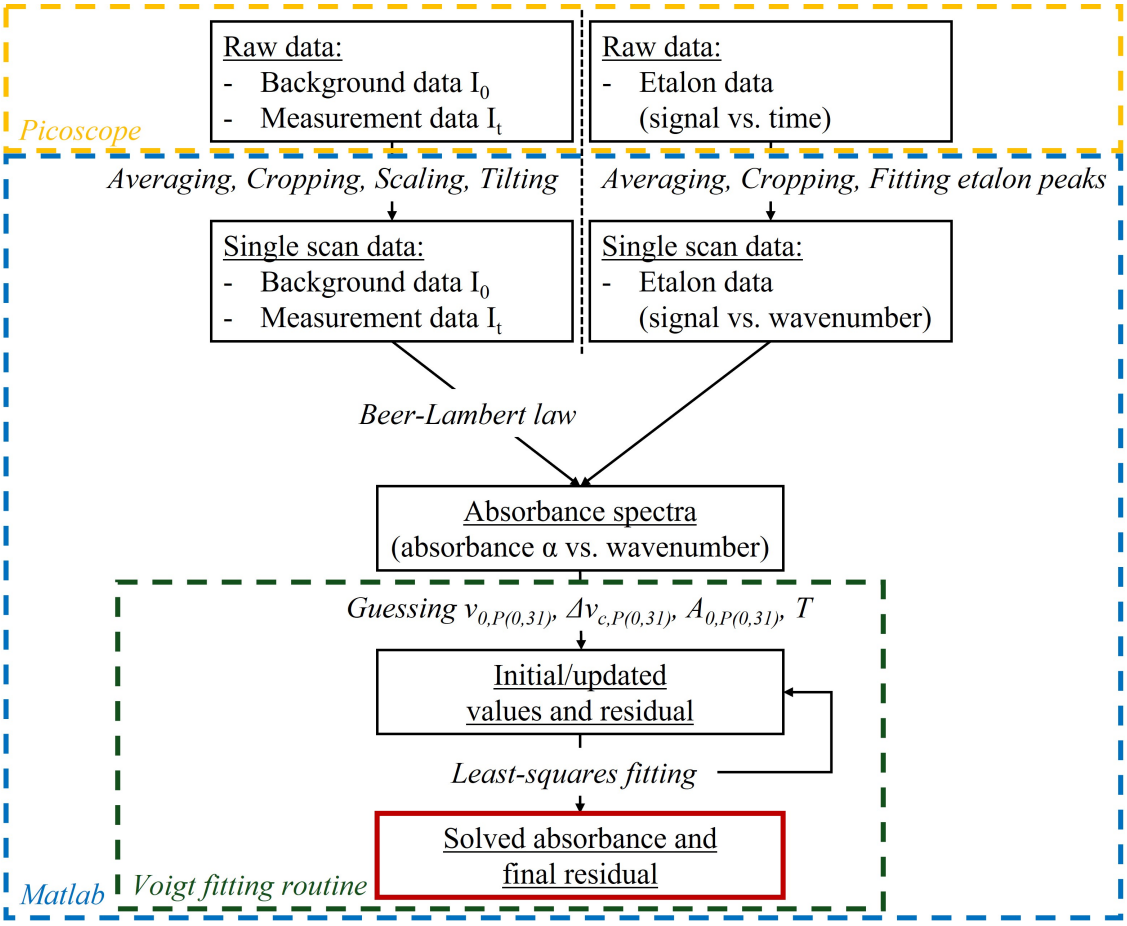

Figure 3.6: Data processing schematic showing the acquisition with the *Picoscope* and the processing as well as the fitting via MATLAB.

The acquisiton in the yellow dashed box is explained more detailed in chapter 4. The actual processing and fitting is done in MATLAB (blue dashed box). First, the raw data including background, measurement and etalon data is averaged and cropped. In the left-hand strand of the figure, the background data is then scaled and tilted in order to better fit the measurement data. The Beer-Lambert law used for the measurement data (transmitted intensity I_t) and the background data (initial intensity I_0) results in the absorbance α, see equation 3.12. In the right-hand strand, the etalon data is transferred from time to wavenumber domain through fitted etalon peaks using a polynomial approach and the Free spectral range (FSR). The FSR is a constant and determined by the etalon material, the resonator length and the wavelength of the incoming light. In the absorbance spectra both strands are merged.

The so called Voigt fitting routine (green dashed box) is the iterative procedure that aims to minimize the residual between measured absorbance spectra and the sum of simulated Voigt profiles. First step is to guess the position ν_0, the collision width ν_c, the area A_0 of the CO line P(0,31) and the temperature T. The characteristics of the other lines P(2,20) and P(3,14) are calculated from these initial values during the routine. A *Least-squares fitting* method provided by MATLAB is used to fit the curve to the measured data. This fitting routine creates updated values for another iteration loop until the residual is reached and the absorbance spectra is solved by a mathematical function which can be investigated through line shape analysis. Major part of this analysis is to extract the line areas from both transitions. This is done through integration of the fitted function and subsequently the division of both areas enables the measurement of temperature and species concentration (see equations 3.17 and 3.19). Such an absorbance spectra with the measured data, the fitted Voigt profile, and the residual is shown in figure 3.7. More detailed information on the Voigt fitting routine can be found in [25].

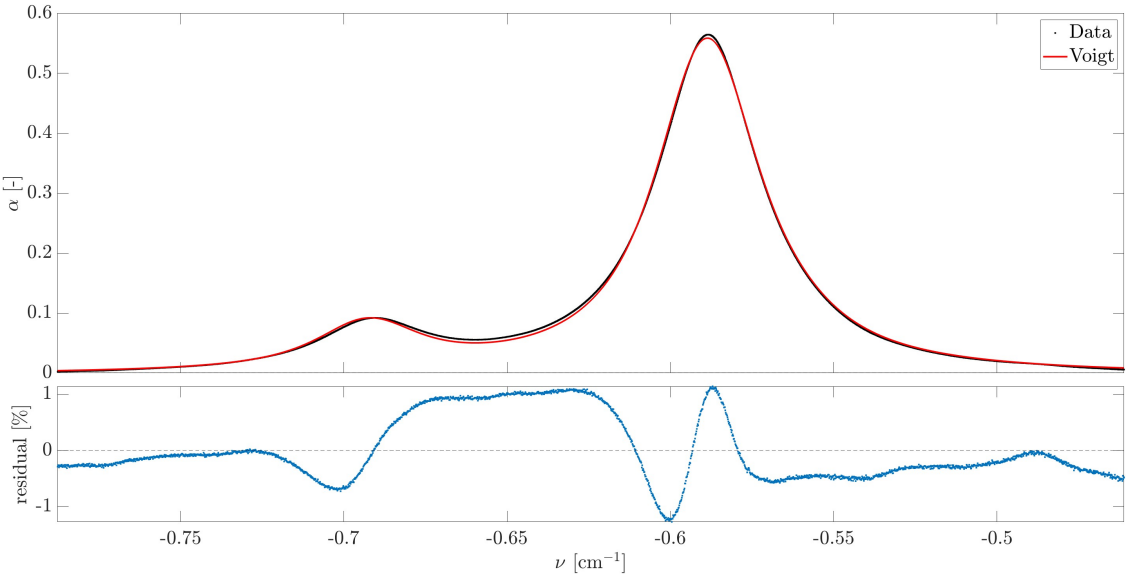

Figure 3.7: Measured absorbance spectra (black markers) and a resulting Voigt fit (red line) with the residual. The underlying data comes from an exemplary 1 kW CH_4 air flame in 1 mm HAB.

3.4 Addition of pure CO

In order to use the same setup for all experiments in this work, some considerations had to be made. The targeted CO molecules are just available in CH_4 flames as intermediate or product species. However, H_2 flames do not provide this molecule. Nair et al. [3] have investigated the possibilty of seeding-in pure CO for pressure measurement in shock tube test facilities. They have not only reached a CO-enriched regime but also found out that the addition of pure CO has negligible effects on ignition timescales. Of course, this application is not directly transferable to the FFB situation but it offers the possibility to use the same experimental setup throughout this work. Therefore H_2 flames are enriched with pure CO in order to obtain temperature data.

As described in chapter 3.3.5, the absorbance should be within a range of $0.1 < \alpha < 2.3$, in best case close to 1. On the other hand, adding too much CO heavily impacts the reaction kinetics of the original H_2 flame. In this field of tension a calculation routine must be developed in order to achieve a decent amount of CO in the flame. In practice, the CO is then added into the fuel supply lines thus takes part in the combustion reactions.

The first step is to push the absorbance of each spectral CO line in the targeted range by floating the species concentration of CO. Figure 3.4(b) is a good example how such an absorbance spectra should look like. The resulting species concentration for CO is added to the simulation code in CANTERA. It calculates a volume flow which can then be set on a Mass flow controller (MFC) in the experiments. This procedure is done for three cases: 21 $vol.\%$ O_2, 50 $vol.\%$ O_2 and 100 $vol.\%$ O_2 and the values in between are exponentially fitted in MATLAB. The resulting volume flow for CO is presented in figure 3.8 and in table 3.3. It can be seen from both that the CO volume flow decreases with higher O_2 ratios. This makes sense because the overall volume flow is decreasing as well and the CO species concentration should remain constant in a range of $1\ vol.\% < X_{CO} < 2.5\ vol.\%$ thus not influencing the reaction kinetics too much.

Figure and table show also CO values for CH_4 flames. In the course of the preliminary tests, the absorbances of these flames were at the lower end of the targeted range. Therefore, additional CO is optimizing the spectra thus increasing the reliability of the data.

Table 3.3: Additional volume flow V_{CO} depending on the O_2 ratio for CH_4 and H_2 flames.

O_2 **ratio in** $vol-\%$	**21**	**25**	**30**	**35**	**40**	**45**	**50**	**75**	**100**
CH_4 **flame:** V_{CO} **in l/min**	0.3	0.27	0.23	0.2	0.18	0.16	0.15	0.11	0.1
H_2 **flame:** V_{CO} **in l/min**	1.4	1.36	1.32	1.28	1.25	1.22	1.2	1.13	1.1

In order to pretest the influence of additional CO on species concentration and temperature the simulation code in CANTERA was used. The results for H_2 flames are presented in figure 3.9. As expected, the influence is significantly which is expressed in temperature differences of approx. 200 K from a HAB of 3 mm. The diagram in figure 3.10 is visualizing the simulated data of CH_4 combustion. The results are very reasonable meaning negligible effect on temperature (~ 20 K) but heavy impact on the CO concentration (increase of ~ 1 $vol.\%$).

The previous considerations about adding pure CO into flames are from a purely theoretical point of view, the experiment on the FFB will show if reality is behaving similar.

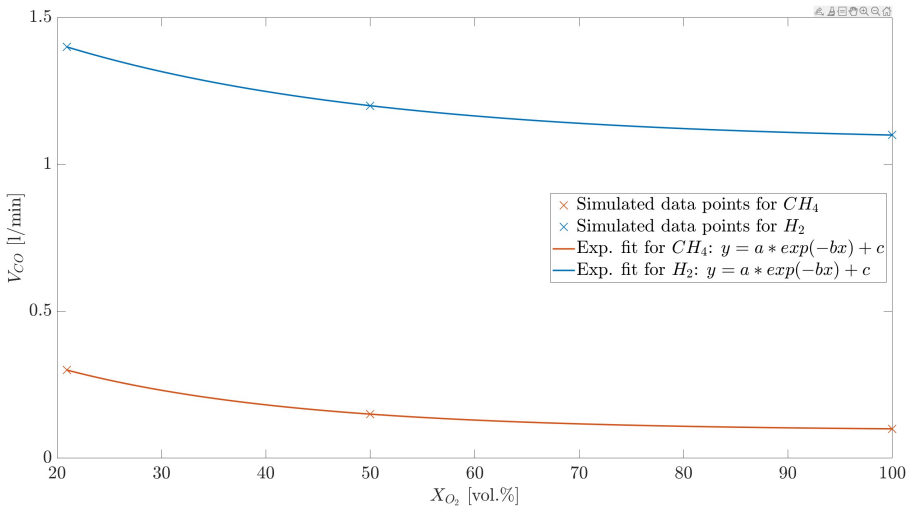

Figure 3.8: Simulated data points for the additional *CO* volume flow and their corresponding exponentially fitted curves (performed in MATLAB).

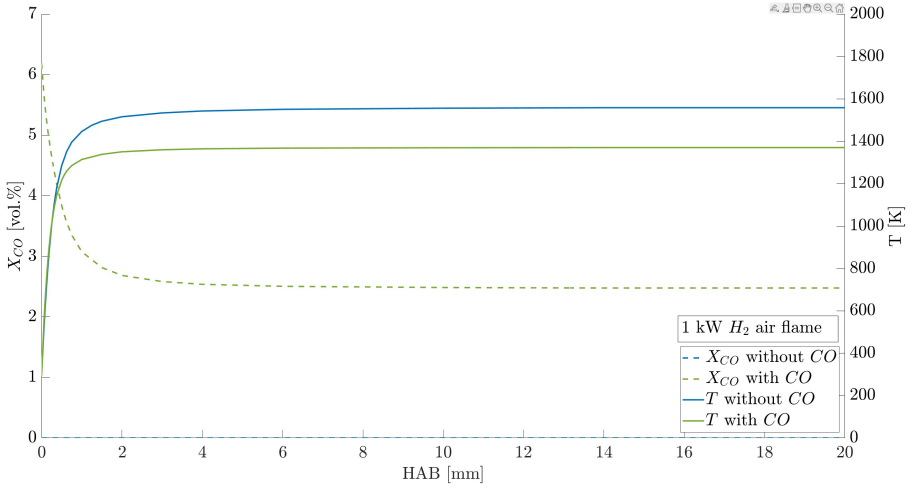

Figure 3.9: Simulated data from CANTERA for a 1 kW H_2 air flame with 1.4 l/min additional *CO* and without *CO*.

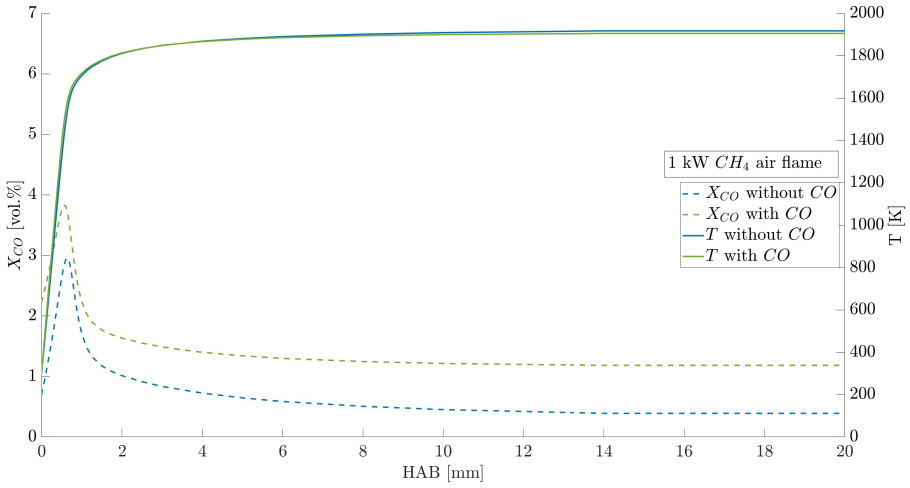

Figure 3.10: Simulated data from CANTERA for a 1 kW CH_4 air flame with 0.3 l/min additional *CO* and without *CO*.

4 Experimental setup

All experiments of this work were performed in the *Laboratory for Gas Dynamics and Laser Spectroscopy* at UCLA. The FFB test stand existed already for flame analysis under vacuum with appropriate low pressure housing but however, the LAS setup was individually ligned up for the purpose of measuring thermodynamic quantities in the flame.

4.1 Flat Flame Burner setup

The FFB was already introduced in detail in chapter 3.1 but some application-oriented information need to be mentioned here. First, the position in the experimental setup is illustrated in figure 4.1 with no. 3. It is mounted on a manually adjustable translation stage which offers the opportunity to measure data along the vertical z-axis. The achievable accuracy by hand is in the range of 0.2 mm. The black lines in the schematic are the fuel/oxidizer and the shroud gas supply lines. The incoming flow is adjusted by MFCs of type *mks GE50A* with different flow rate ranges and sealants depending on the gas that needs to be regulated. The brown lines, representing copper, are the cooling water circuit that is operated with laboratory water at ambient conditions. The flow rate is fixed at 0.44 l/min for all experiments. No. 2, the black rectangles with grey knobs are irises that are mounted on both sides of the housing. This ensures that the laser light is aligned through the vertical center axis of the burner. The grey marked housing is from the vacuum setup and helps to keep conditions stable and free from disturbances, e.g. ambient air/wind. At the sides, the housing is open for the laser light and at the top for the exhaust gases thus ambient conditions prevail.

On the left of the FFB is the laser and on the right the detector with several optical devices in between. These are presented in the next chapter.

4.2 Laser absorption spectroscopy setup

The LAS setup is also shown in figure 4.1. More precisely stated, it is *scanned-wavelength direct absorption* meaning this technique spans a narrow region of the spectrum from 0.1 to 10 cm^{-1} in wavenumber to resolve one or more absorption transitions [26]. This region can be slightly shifted through change in laser temperature or injection-current tuning.

The laser in this setup works exactly according to this functional principle meaning it is characterized through rapid tunability and futhermore, a compact size. It is a so called Quantum-cascade laser (QCL) from *Alpes Lasers* and is illustrated in figure 4.1 on the left with no. 1. The laser

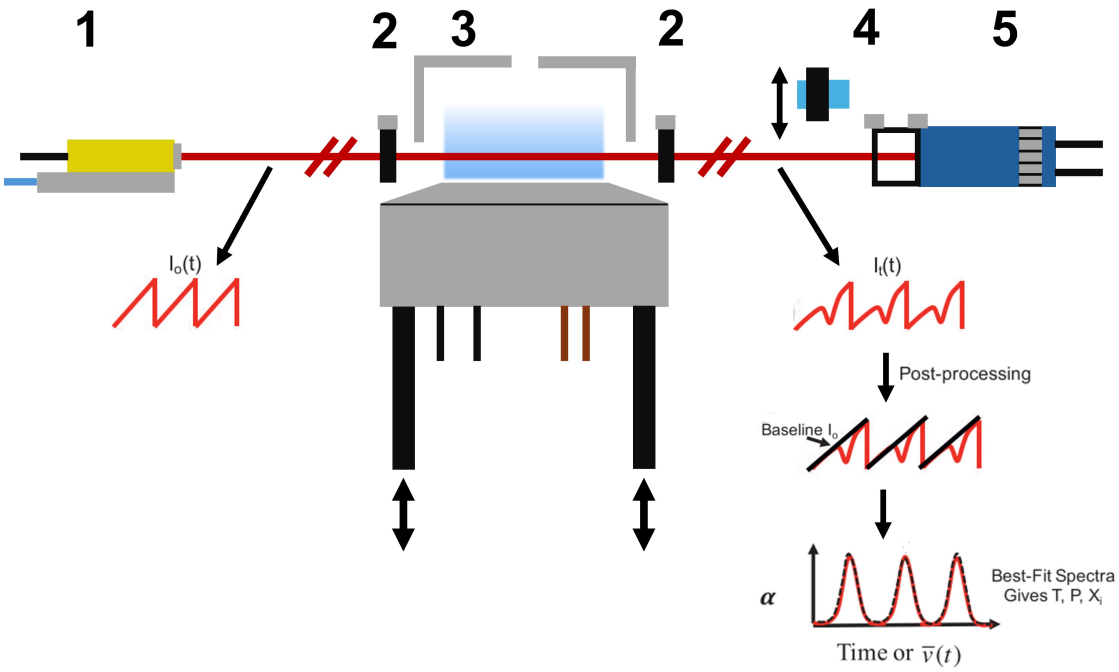

Figure 4.1: Experimental setup showing the FFB and relevant devices for the LAS.

cooling circuit is fine tuned with a thermoelectric cooler integrated in the housing and supported by an external cooling source (base with blue supply). The injection current is provided by a power source which is then superimposed with a sawtooth function by an adequate generator. The frequency used in this work is 6.25 kHz.

Following the laser light in the figure, silver mirrors would be the next optical device but are neglected here for better visibility. The irises (no. 2) ensure a straight alignment through the flame axis and on the other side of the FFB the original intensity is attenuated by the part that is absorbed by the *CO* molecules. No. 4 represents a moveable etalon which is made of Germanium. Between the entry and exit surfaces of the etalon a standing wave is created, which can be recorded on the detector (no. 5) in a separate experiment. Ahead of the photovoltaic detector from *Vigo* is another pair of irises which ensures a perpendicular entry of the attenuated laser light. Finally, the detected intensity is transferred into a voltage signal and forwarded to the *Picoscope* which displays the signal over time.

The data acquisition steps are roughly indicated in the figure with schematics but a detailed description is given in the following chapter.

4.3 Data acquisition

The theory behind this procedure is shown in figure 3.6 while the focus here is more on concrete steps for acquiring the data in practice.

In this work, the raw data is recorded over a period of 50 ms and then averaged to a single scan. This is done with all signals meaning the background, etalon and measurement data and the

results can be seen in figure 4.2. The flame is fueled with H_2 and air and shows a representative voltage signal over time. The three signals correspond to the three major steps that are part of every LAS measurment in order to acquire data: (i) First step is a background signal measurement (black curve) which corresponds to the initial intensity $I_0(t)$. Therefore, the flame has to be turned off and the unattenuated signal goes through the alignment and is recorded by the detector. (ii) Next step is the etalon measurement acquired also with the burner turned off. The standing wave can be clearly seen in the green signal. Calculated with the FSR, it gives the opportunity to switch from time to wavenumber domain. (iii) The measurement signal contains the data of interest which is specific for the targeted species. Obviously, the flame has to be ignited and become stationary (~ 1 min). Then the absorbance features have fully formed and can be recorded. A general rule of thumb is that the features should be in the right part of the scan for higher resolution and larger reserve to saturation of the detector. The scan shows that the laser parameters are selected decently.

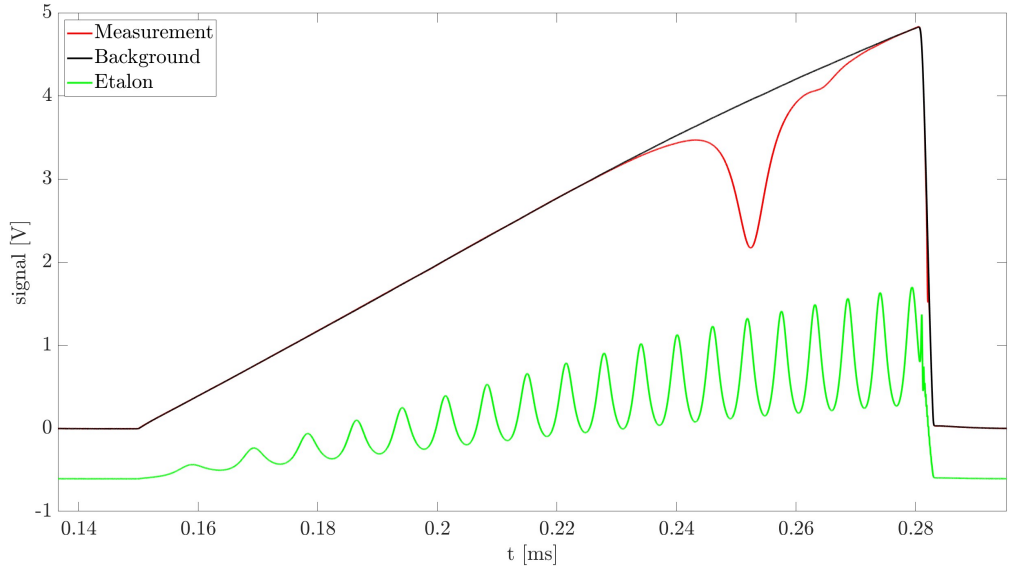

Figure 4.2: Raw data of the measurement, background and etalon signal of a single scan before time-to-wavenumber transition (1 kW H_2 air flame in 1 mm HAB).

After accomplishing all data processing steps from 3.6, the final spectra of *CO* is presented in figure 4.3. It shows the absorbance over wavenumber and the corresponding residual between the data points and the fitted Voigt profile.

After extracting the areas under the *CO* absorbance features the temperature and species concentration can be determined. This is done from 1 mm up to 20 mm HAB. This range has been defined because the flame behaves turbulently above it thus makes the measurements unreliable. For higher O_2 ratios the experiments were discontinued at lower HABs because the transition point moves closer to the burner surface. In order to meet the steep reaction gradients in the flame zone at low HABs, a higher resolution was selected meaning more data points were acquired. However at higher HABs, smaller changes led to the decision of reducing the resolution thus reducing experimental efforts. Figure 4.4 shows the profile over the full HAB.

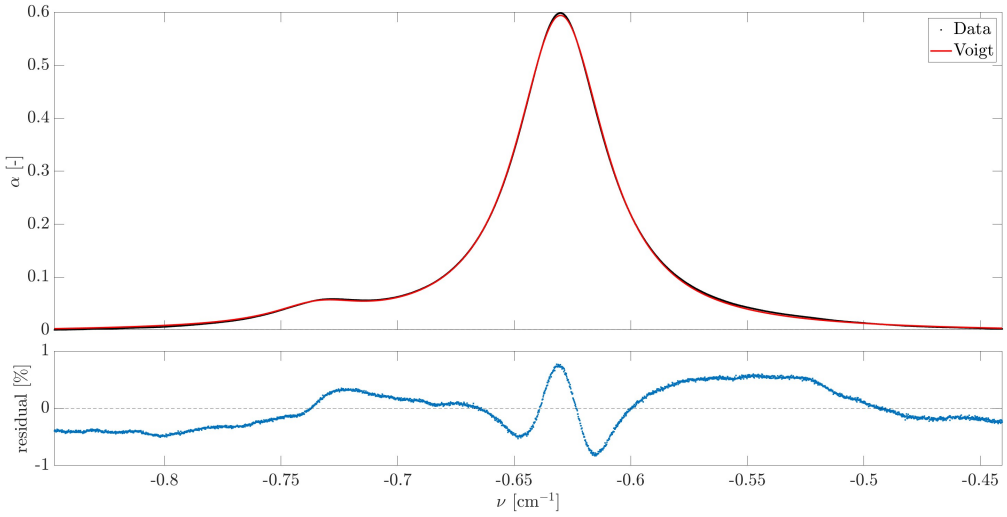

Figure 4.3: The upper diagram displays the measured absorbance spectra, illustrated through black data points, from a 1 kW H_2 air flame (1 mm HAB) and red Voigt line fit. The lower diagram shows the resiudal between these two. The x-axis shows the relative wavenumber after time-to-wavenumber transition.

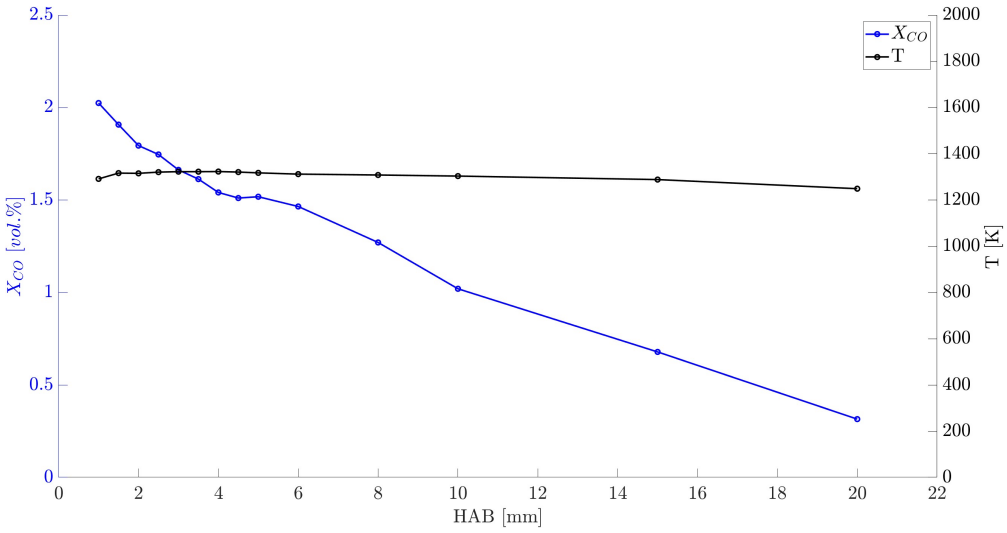

Figure 4.4: Temperature and CO species concentration for a 1 kW H_2 air flame over the full measured HAB.

4.4 Test parameters and matrix

A lot of pre-tests had to be performed in order to find the right parameters for the main experiments, e.g. finding a reasonable thermal output power for the flame of the FFB, validating the calculated volume flow rate for the additional CO, measuring the absorbance in reliable HABs, finding reasonable parameters for laser temperature and current, a suitable injection-current function for the LAS setup, checking the reproducibility and many more. The main experiments consist of varying the O_2 content in the oxidizer for various HABs in CH_4 and H_2 flames.

The identified parameters for the main experiments are concluded and listed, at a glance, in the following. They are the preconditions for the test matrices of CH_4 and H_2 which are presented below in table 4.1 and 4.2.

FFB:

- 1 kW thermal output power P_{th} for all experiments (neglecting additional CO)
- Fuel: separated CH_4 and H_2 fueled flames
- Oxidizer: synthetic air with increasing O_2 ratios from 21 - 100 vol.% O_2
- Equivalence ratio ϕ = 1.0
- No shroud gas
- Constant cooling water volume flow: 0.44 l/min
- Measurement range above the burner: 1 - 20 mm if the turbulent transition point allows it
- Additional CO volume flow for CH_4: 0.3 - 0.1 l/min for higher O_2 ratios
- Additional CO volume flow for H_2: 1.4 - 1.1 l/min for higher O_2 ratios

LAS:

- Mean injection-current: 90 mA with superimposed sawtooth function with 1.4 $V_{peak\text{-}to\text{-}peak}$
- Laser output power: 50 mW peak power
- Thermoelectric cooling temperature of the laser: 10.0 °C
- Wave length of the laser light: ~ 4.98 µm
- Laser tuning range: here ~ 2008 - 2009 cm⁻1 (overall: ~ 2001 - 2012 cm⁻1)
- Laser measurement rate: 6.25 kHz
- Detector sample rate: 200 MHz
- Software recording parameters: 62.5 MS/s for 50 µs on a 15-bit scale

Table 4.1: Test matrix for CH_4 flames. All experiments were performed (if possible) from 1 - 20 mm HAB.

$vol - \%\ O_2$	21	25	30	35	40	45	50	75	100
V_{CH_4} in l/min					1.68				
V_{O_2} in l/min					3.35				
V_{N_2} in l/min	12.65	10.06	7.82	6.23	5.02	4.10	3.35	1.12	0
V_{CO} in l/min	0.3	0.27	0.23	0.2	0.18	0.16	0.15	0.11	0.1

Table 4.2: Test matrix for H_2 flames. All experiments were performed (if possible) from 1 - 20 mm HAB.

$vol - \%\ O_2$	21	25	30	35	40	45	50	75	100
V_{H_2} in l/min					5.56				
V_{O_2} in l/min					2.78				
V_{N_2} in l/min	10.49	8.34	6.49	5.16	4.17	3.40	2.78	0.93	0.00
V_{CO} in l/min	1.4	1.36	1.32	1.28	1.25	1.22	1.2	1.13	1.1

5 Results and discussion

The following chapter is dedicated to the results obtained in this work. As mentionend in the introduction, two specific cases are of interest: (i) O_2 enriched flames and (ii) the fuels CH_4 and H_2. In order to be able to evaluate the data, the basis is an analysis of uncertainty and reproducibilty. After that, the aim is to draw conclusions and trends in the measured data and compare them with the simulation. Furthermore, the results are checked on plausibility and critically discussed thus methodological improvements can be made for future works.

5.1 Uncertainty and reproducibility

The knowledge of uncertainty and reproducibility is a relevant requirement to investigate the changes in results when one parameter is varied. In this work, the most important sources of errors are briefly outlined, more detailed uncertainty analysis is presented in the literature [2, 3, 23]. Kuenning et al. [19] have presented a decent uncertainty analysis for measuring temperature and species concentration with the same CO lines. Figure 5.1 (a) and (b) are taken from their work and give an orientation to be able to estimate the error range.

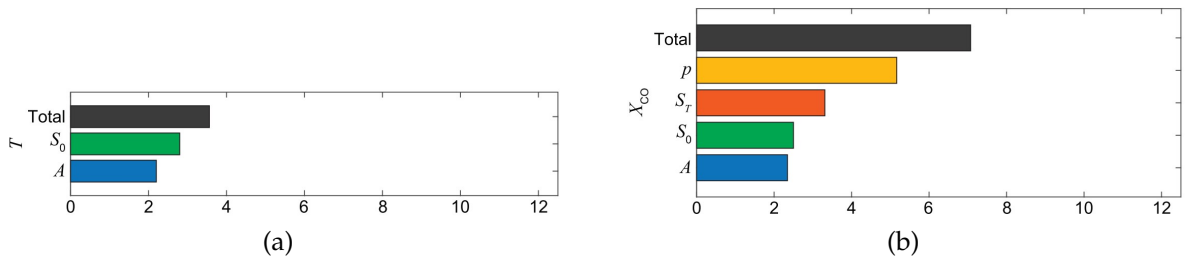

Figure 5.1: (a) Representative uncertainty for the temperature T, (b) Representative uncertainty for the species concentration X_{CO}, both figures (a) and (b) taken from Kuenning et al. [19].

The lineshape related uncertainty of temperature measurement primarily stems from the Boltzmann population fit which is heavily influencend by two major aspects: (i) uncertainty in the three CO line areas A and (ii) uncertainty in the reference line strength $S_0(T)$. Aspect (i) represented through the blue error bar in figure 5.1(a) is considered through the fit residual. It is plotted for every evaluation and is always < 2%. Among other things, this aspect includes the Voigt fitting uncertainty and the assumption that all CO lines have the same line width. In order to quantify aspect (ii), the concrete CO reference line strength uncertainties are: 5% for P(2,20), 2% for P(0,31), and 10% for P(3,14) These errors are available in the HITEMP database [27] for most lines. The cumulated error is illustrated by the green bar. The total error (black bar) is within a range of 3 -

4%. In this work the fit residual is even better in most cases (around 1%) thus a decent total error should be around 3%.

The uncertainty of species concentration is a combination of the previously presented line areas A and reference linestrengths $S_0(T)$ with the temperature-dependent linestrengths $S_T(T)$. The temperature-dependent linestrength uncertainty is a result of the previously calculated temperature uncertainty. In the work of Kuenning et al. [19], see figure 5.1(b), pressure is leading to a higher uncertainty because it is one of the unknowns. This does not apply to this work because pressure is a known variable since all experiments were conducted under athmospheric conditions. Concludingly, the total error for species concentration is definitely < 7%. A decent estimation would be around 5%.

Besides these more spectroscopic aspects, there are experiment related uncertainties caused by the FFB or the LAS alignment. Therefore, an exemplary CH_4 air flame was investigated in 1, 3, 5, 10, 15 and 20 mm HAB five times without changing any parameters. This procedure allows statements to be made about reproducibility. The results are presented in figure 5.2. In low HABs, the reproducibility is best for species concentration as well as temperature. In higher HABs, the uncertainty increases due to the turbulent behaviour of the flame. Since the timescale of this turbulent behaviour is slower than the measurement timescale, the experimental data fluctuates. For higher O_2 ratios the transition point from a laminar to a turbulent flame moves closer to the burner surface because of a decreasing overall volume flow. Therefore, flames with 100 vol.% O_2 were just measured up to 5 mm HAB. However, the temperature measurement is very valid, as the uncertainty almost exclusively is of systematic origin while the reproducibility has a nearly neglectible impact. For species concentration, the situation is different because the reproducibilty dominates the uncertainty.

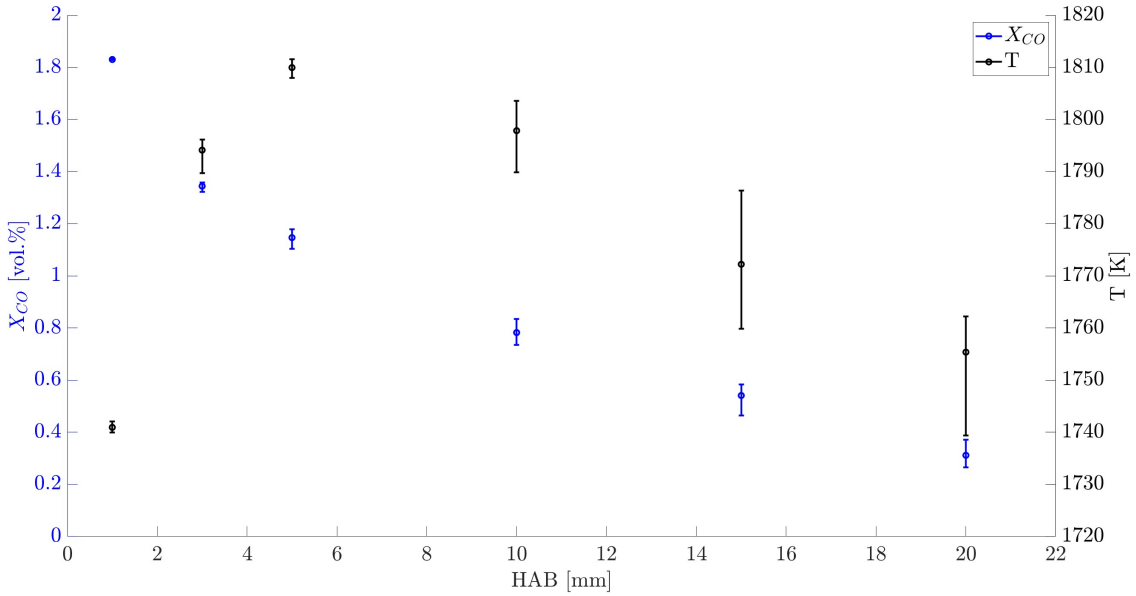

Figure 5.2: Reproducibility of temperature and CO species concentration of an exemplary CH_4 air flame investigated five times at various HABs.

In order to get a total relative uncertainty both lineshape and reproducibilty must be added. The results with the final values are shown in table 5.1 and 5.2.

Table 5.1: Total uncertainty for CO species concentration measured in this work.

HAB [mm] / **Uncertainty [%]**	1	3	5	10	15	20
Lineshape	~5.00					
Reproducibility	0.14	1.06	2.42	4.85	9.10	16.59
Total for X_{CO}	**5.14**	**6.06**	**7.42**	**9.85**	**14.10**	**21.59**

Table 5.2: Total uncertainty for temperature measured in this work.

HAB [mm] / **Uncertainty [%]**	1	3	5	10	15	20
Lineshape	~3.00					
Reproducibility	0.05	0.14	0.07	0.29	0.57	0.56
Total for Temperature	**3.05**	**3.14**	**3.07**	**3.29**	**3.57**	**3.56**

5.2 General trend of the data

The test series conducted in this work dealt with CH_4 and H_2 flames while increasing the oxidizer's O_2 ratio from 21 up to 100 vol.% O_2. Through the increase of the O_2 ratio, the overall efficiency of the combustion should also increase which is expressed through higher flame temperatures. The reason for higher temperatures is less N_2 in the oxidizer. N_2 takes part in the combustion reaction and must be heated up, in order to reach an ignitable mixture. The heat energy is "lost" instead of increasing flame temperature. In theory, a 100 vol.% O_2 flame consists only of fuel and oxidizer and the highest flame temperatures are reached. Figure 5.3 and 5.4 show all data acquired in this work. In the following, these diagrams are analyzed from the oxidizer and then from the fuel perspective.

5.2.1 Influence of O_2 ratio

Figure 5.3 (b) shows data from the CANTERA simulation code for CH_4 flames and reflects exactly the expected behavior. Lowest temperature for 21 vol.% O_2 and highest temperature for 100 vol.% O_2. Also the ignition point moves closer to the burner surface for higher O_2 ratios and a stronger gradient can be observed which results in higher flame temperatures right from the start. Figure 5.3 (a) shows the measured data but however, the expected effects cannot be verified at all. A contradictory behaviour is more likely to be seen here. Lowest temperature for 100 vol.% O_2 and highest temperature for 21 vol.% O_2. An explanation is that the overall volume flow decreases with higher O_2 ratios which leads to lower flow velocities of the gas. This results in an ignition point closer to the burner surface which causes the porous burner plug to heat up while reducing the flame temperature. In fact, reducing the flow velocity is one method to reduce the flame temperature. Better methods for flame temperature control are (i) the cooling waterflow through the burner plug which simply transports the heat away and (ii) replacing the oxidizer's N_2 with

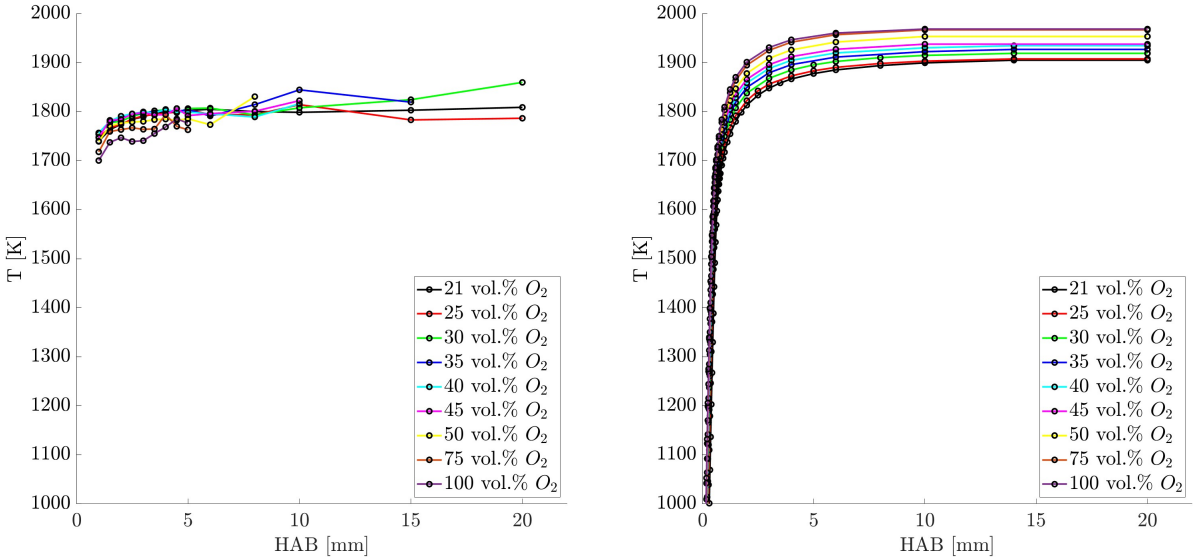

(a) (b)

Figure 5.3: (a) Measured temperature data of oxygen enriched CH_4 flames, (b) Simulated temperature data of oxygen enriched CH_4 flames.

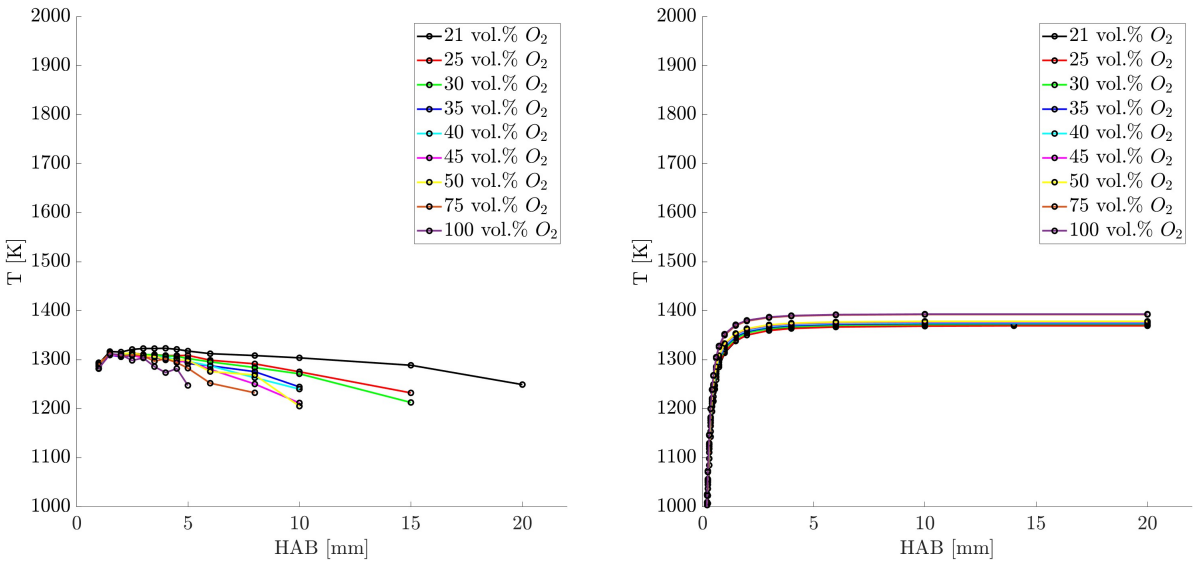

(a) (b)

Figure 5.4: (a) Measured temperature data of oxygen enriched H_2 flames, (b) Simulated temperature data of oxygen enriched H_2 flames.

Ar. These methods are extensively outlined in the literature [28, 29]. At this point it must be stated that the FFB in this configuration is not the appropriate burner type to proove higher flame temperatures due to higher O_2 ratios. Coming back to method (ii) meaning *Ar* instead of N_2 could be a promising approach to investigate higher O_2 ratios.

The same behavior can be found with H_2 flames which are visualized in figure 5.4(a) and (b). The simulated data reveals the expected phenomena but the measured data is contradictory.

5.2.2 Influence of fuel

The figures 5.3 and 5.4 illustrate more interesting aspects in particular when analyzing the differences between CH_4 and H_2. At first glance, the measured and simulated data seems to contradict coincidently the Adiabatic flame temperature (AFT) of CH_4 and H_2, see table 5.3. Of course, it has to be considered that more CO was seeded into the H_2 flames lowering their temperatures. But even for CO free flames CANTERA predicts higher flame temperatures for CH_4. This can be seen in figure 3.9 and 3.10. However, for a burner stabilized flame as it is simulated and measured here, the comparison with the AFT is misleading.

Burner-stabilized flames work differently. As previously explanined in chapter 3.1, the LBV plays an important role and it differs between CH_4 and H_2 by a factor of approx. 6 while the flow velocity v_{exit} remains approx. the same, see table 5.3. Simply stated, the direction of the LBV is opposite to the flow velocity of the gas meaning for a burner-stabilized flame that the reaction front constantly tries to move upstream. The FFBs porous plug acts as a barrier so that the flame front is stabilized above the burner surface. The higher LBV of H_2 is leading to a stronger upstream drive and an earlier ignition of the mixture meaning much closer to the burner plug. The burner cooling removes more heat, which lowers the flame temperature. This phenomenon was also evident during the test phase. For H_2 with 100 vol.% O_2 the burner plug started to glow but not for CH_4 under the same conditions, see figure 5.6 (b). The previous explanations also apply in reverse to CH_4 which allows the flame to burn hotter. All physical properties listed in table 5.3 refer to air flames but the trend is generally applicable also for higher O_2 ratios [30].

Another aspect seen in the figures is the decrease in temperature at higher HABs. The CH_4 temperature curves are nearly stable along the vertical axis while the H_2 curves decrease. One explanation is again the higher LBV which is a result of faster reaction kinetics. H_2 as the fuel is faster processed in a narrow reaction zone which is characterized by strong gradients. In greater HABs, the flame already cools down. A secondary approach are the combustion products H_2O and CO_2 which are formed by the elementary oxidation reactions of CH_4 and H_2, displayed in table 5.3. Not only H_2O has a higher heat emission coefficient ϵ over a broad range of temperature and wavelength also the species concentration is much higher for H_2 combustion [31]. This leads to overall higher radiation losses causing the flame to cool down faster. The radiation effects can not be seen in the simulation data because the radiation model was intentionally disabled.

Table 5.3: Relevant elementary physical properties of CH_4 and H_2 air flames, taken from CANTERA [4].

Fuel	CH_4	H_2
Oxidation reaction	$CH_4 + 2\ O_2 \rightarrow CO_2 + 2\ H_2O$	$2\ H_2 + O_2 \rightarrow 2\ H_2O$
X_{H_2O} **[vol.%]**	18	26
X_{CO_2} **[vol.%]**	9	0
flow velocity v_{exit} **[cm/s]**	11.46	10.89
LBV v_L **[cm/s]**	37.34	236.22
AFT $T_{adiabat}$ **[K]**	2227	2382

5.2.3 Influence of additional *CO*

The influence of additional *CO* was already investigated theoretically in chapter 3.4 while the focus here lies on the influence of *CO* in reality. Therefore in figure 5.5 (a), a CH_4 air flame with and without additional *CO* is presented.

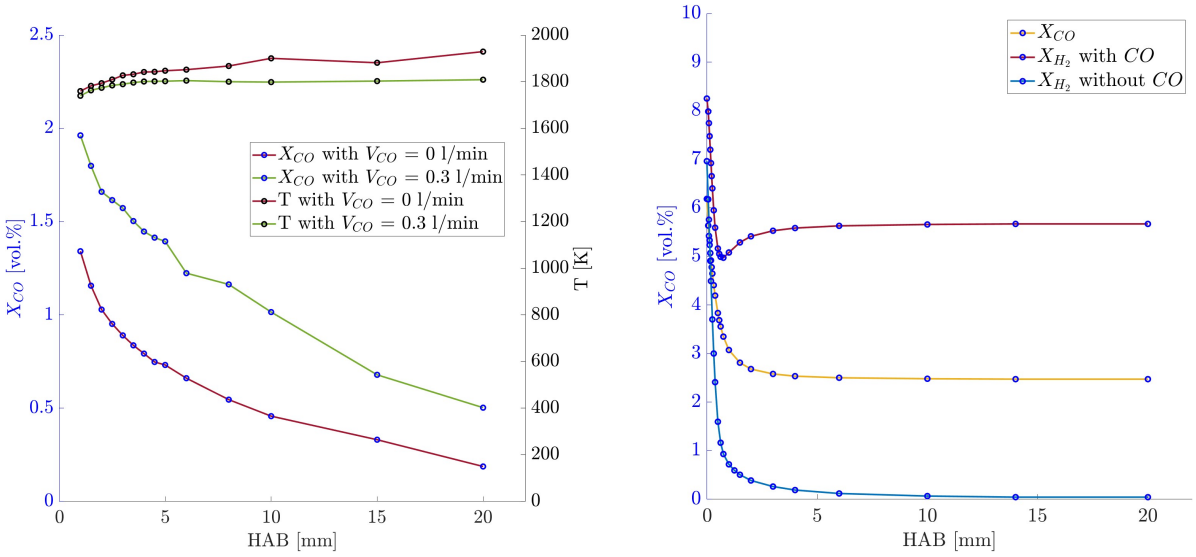

Figure 5.5: (a) Influence of additional *CO* on temperature and species concentration in a CH_4 air flame, (b) Changes in residual species concentration of H_2 when *CO* is added.

The results show that the addition of pure *CO* worked perfectly for CH_4. While not influencing the temperature too much (~ 50 K) the species concentration was increased by approx. 1%. This moves the absorbance of the *CO* lines in the targeted range so that a valid measurement was enabled. Furthermore, the simulation data from figure 3.10 agrees well with the measurement data shown here. Obviously, such a comparison cannot be made for H_2 because the LAS setup used in this work is customized to *CO*. But nevertheless, it can be concluded from the simulation that additional *CO* is influencing the reaction kinetics of H_2 flames significantly. Figure 5.5 (b) demonstrates the species concentration of H_2 and *CO* along the vertical burner axis. With additional *CO*, a residual content of H_2 (~ 6%) and *CO* (~ 2.5%) leave the reaction zone unprocessed. This causes the flame temperature to decrease because the full potential of the fuels is not utilized. It seems that H_2 and *CO* compete for O_2 which is only available to a limited extent since the FFB flame is premixed. Without additional *CO*, H_2 is completely processed.

For CH_4 flames *CO* is a decent molecule for temperature measurement but for future applications burning H_2, another molecule should be targeted.

5.3 Validation of the data

The validation of the data by other sources is the focus of this chapter. In general, the data situation in the literature for O_2 enriched flames on a FFB is rather sparse. Many experiments were carried

out with other overall volume flows, fuels or equivalence ratios which affects the comparability. Often the FFB was more a tool to demonstrate sensors instead of investigating the flame itself meaning the goals of the works differ a lot from each other. Therefore the focus here was limited to air flames where the data situation is better. In the further course of this chapter, the measured data will be compared in detail with the simulation.

5.3.1 Comparison with literature

A look at the literature (see table 5.4) confirms the temperature data obtained in this work. Yang et al. [32] measured temperature with broadband absorption spectroscopy and Weigand et al. [33] as well as Prucker et al. [13] used Coherent anti-Stokes Raman Scattering (CARS). The measured temperature for a H_2 flame lies at 1300 K due to the additonal CO. However, the simulation reveals that a pure H_2 flame temperature in this configuration is approx. 200 K hotter, i.e. 1500 K (from figure 3.9). If this circumstance is taken into account, the data from this work looks much more valid (deviation approx. 65 K). Therefore, the corrected value (*) is listed in table 5.4. The flame temperatures of CH_4 flames show decent agreement with the literature and are in the uncertainty calculated in this work.

Table 5.4: Comparison of exemplary CH_4 and H_2 flame temperatures with the literature.

Literature	**T (CH_4 air) [K]**	**T (H_2 air) [K]**	**T (Urban) [K]**	**HAB [mm]**
Yang et al. [32]	~1750	-	**1790**	3
Weigand et al. [33]	~1790	-	**1810**	15
Prucker et al. [13]	-	~1565	**~1500***	15

*corrected value

5.3.2 Comparison with 1D-simulation

This chapter goes more into detail on the simulation performed in CANTERA to display strengths and weaknesses. Therefore several diagrams (figure 5.7 - 5.12) were plotted starting from 21 up to 100 vol.% O_2 for both CH_4 and H_2. Temperature and the CO species concentration are displayed because both variables are inferred independently thus allow an independent validation, as already explained in chapter 3.3.4. For both measurement and simulation the addition of pure CO was considered so that the comparability is ensured.

Figure 5.7 (a) and (b) show measured and simulated air flames (21 vol.% O_2). For CH_4, the agreement is good for temperature and excellent for the species concentration, in particular close to the burner surface. In higher HABs, a larger deviation must be noted due to diffusion effects with the real environment. Moreover, all experiments were conducted without shroud gas. So not only heat energy is released lowering the temperature but also CO lowering the species concentration. In addition, the FFB might not be as homogeneous as assumed. In the course of the preparation of this work, OH* chemiluminescence images were recorded. Figure 5.6 (a) shows a CH_4 air flame with an uneven OH* distribution which generally also indicates an uneven

temperature distribution. This could also lead to a deviation since in this work, temperature was only obtained along the center axis of the burner. On the other side, the simulated scenarios are performed in an ideal, closed, homogeneous and adiabatic reaction domain. This systematic deviation explains to some extent the differences thus cannot be prevented.

It is rather the opposite for H_2. The agreement for temperature is excellent and the same reasoning as for CH_4 also applies to H_2 explaining the lower simulation temperatures in higher HABs. However, the species concentration deviates relatively strong. Close to the burner surface, the simulated CO is processed but above 5 mm the concentration remains constant while the reality shows a nearly linear decrease. In conclusion, it can nevertheless be said that the deviation for temperature is in a range of 50 - 100 K which is a decent value. CO species concentration is almost perfect for CH_4 but, however, worse for H_2. The fuel seems to have an influence here.

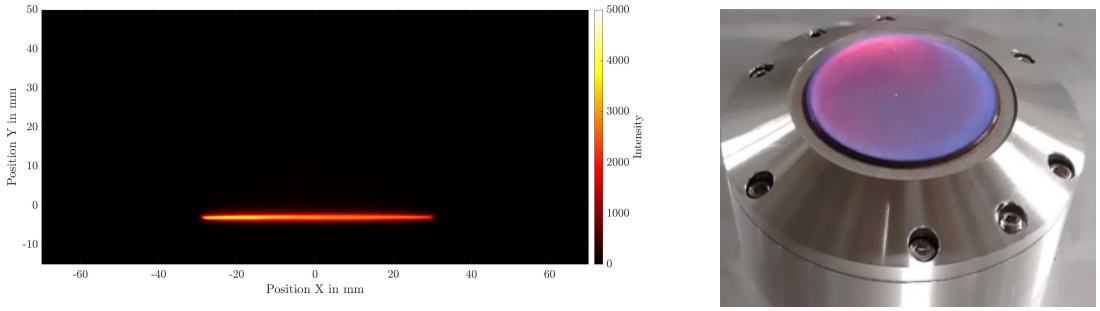

(a) (b)

Figure 5.6: (a) OH* image showing a slightly uneven distribution along the burner plane, (b) For H_2 flames with high O_2 ratios the porous burner plug starts to glow.

For all other diagrams in figures 5.8 - 5.12, the deviations tend to become stronger. This is mainly due to the fact that the overall volume flow decreases with higher O_2 ratios which reinforces the already mentionend mechanism of heat transfer to the burner plug. In particular, the measured CO species concentration in H_2 flames deviates significantly. The reaction mechanism used in this work cannot be the origin because the comparison from chapter 2.1 has shown that this occurs in all cases. It seems that the mechanisms underestimate the reaction involvement of CO in C-free fuels in general because the prediction of CO in CH_4 is much better. Another approach could be again mass transfer with the environment which would lower the CO species concentration as well.

When taking a final look on the measured and simulated data, it can nevertheless be stated that the similarities predominate. In particular, for the air flames the simulation shows decent predictions. For higher O_2 ratios, the experimental setup should be adapted. Adequate suggestions for improvement are presented in chapter 6.

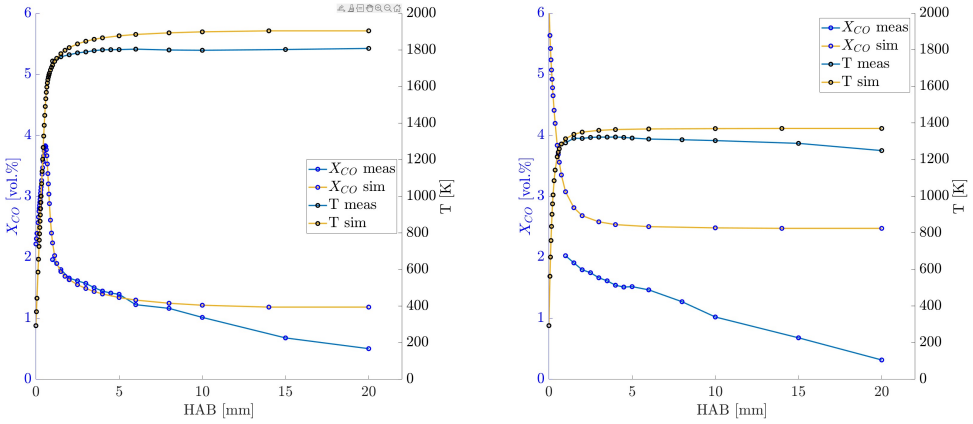

(a) (b)

Figure 5.7: Comparison of simulated and experimental data of CH_4 (a) and H_2 (b) flames with 21 vol.% O_2.

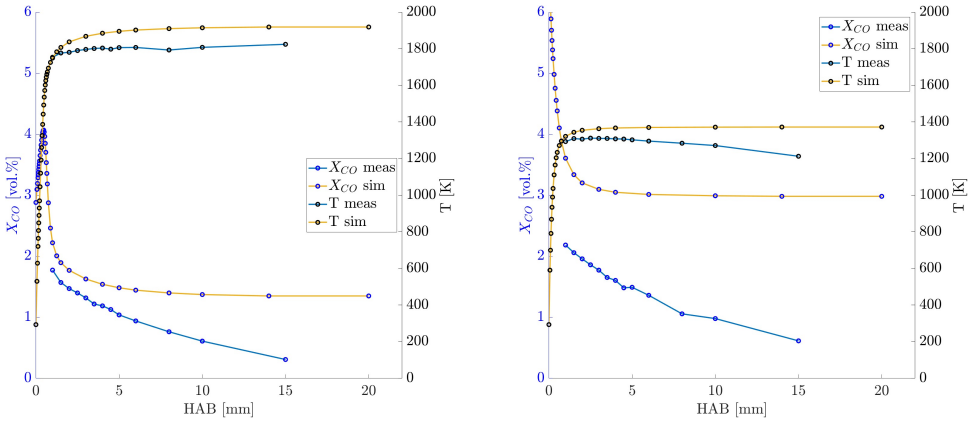

(a) (b)

Figure 5.8: Comparison of simulated and experimental data of CH_4 (a) and H_2 (b) flames with 30 vol.% O_2.

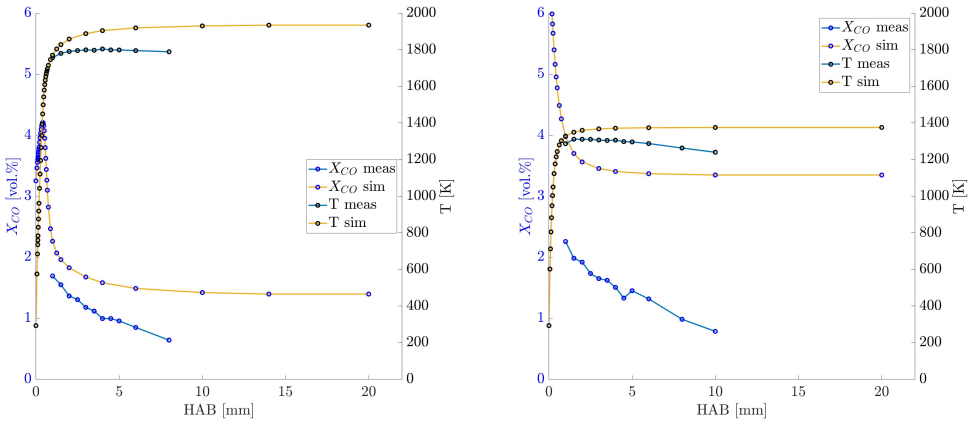

(a) (b)

Figure 5.9: Comparison of simulated and experimental data of CH_4 (a) and H_2 (b) flames with 40 vol.% O_2.

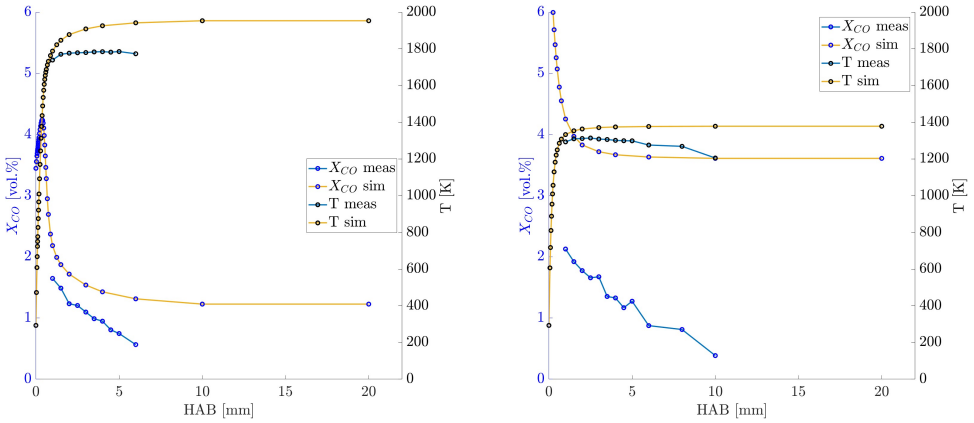

(a) (b)

Figure 5.10: Comparison of simulated and experimental data of CH_4 (a) and H_2 (b) flames with 50 vol.% O_2.

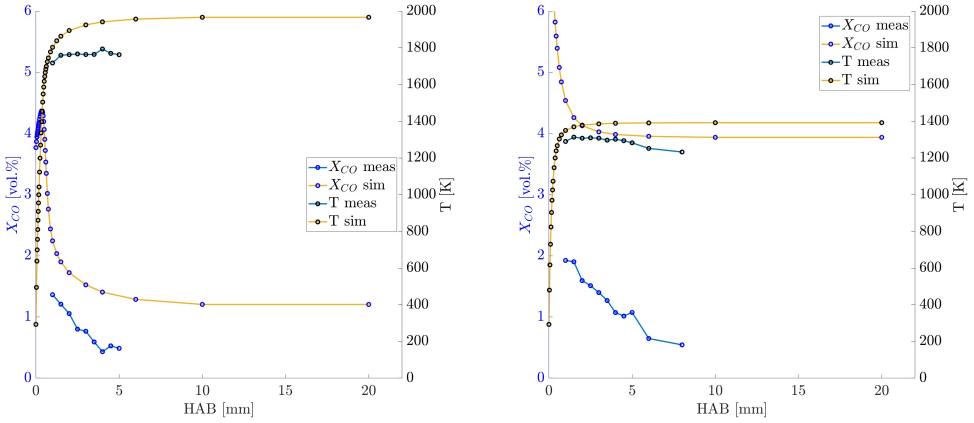

(a) (b)

Figure 5.11: Comparison of simulated and experimental data of CH_4 (a) and H_2 (b) flames with 75 vol.% O_2.

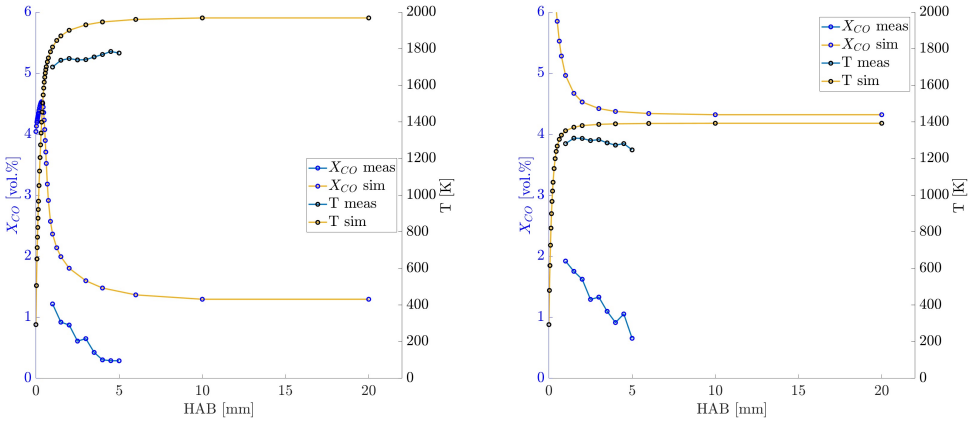

(a) (b)

Figure 5.12: Comparison of simulated and experimental data of CH_4 (a) and H_2 (b) flames with 100 vol.% O_2.

6 Conclusion and outlook

A premixed and burner-stabilized flat flame was investigated in this work using LAS to measure temperature and afterwards validated through a 1D-simulation in the computational framework of CANTERA.

The two initial goals were to study the influence of the fuels CH_4 and H_2 as well as O_2 enriched oxidizers. The basis for the experimental part was a laboratory scale FFB which was located in the *Laboratory of gas dynamics and laser spectroscopy* at UCLA. The LAS setup was aligned through the vertical center axis of the FFB and targeted at CO. The test series started at 21 vol.% O_2 up to 100 vol.% O_2 for both CH_4 and H_2. During such a test, the burner was translated vertically to measure in a range from 1 mm up to 20 mm HAB. For each HAB, a CO absorbance spectra from 2008 cm^{-1} to 2009 cm^{-1} was recorded which allows to infer temperature and CO species concentration. Moreover, all combustion scenarios were parallel simulated to validate the experimental results.

First of all, the uncertainty in particular close to the burner surface was very low which makes the data reliable. In higher HAB, it remained constantly low for temperature but increased for the CO species concentration. For future applications, it would be an advantage to know more about the flow behaviour of the burner. This allows to better estimate where the transition point between laminar and turbulent flame is because this influences the uncertainty of the data. A promising workaround could also be to adapt the data acquisition, i.e. record data over a longer timescale to average the turbulences. The timescale of this work was perfect for the laminar area of the flame but could have been increased for higher HABs to better meet the challenges of a turbulent flame.

Regarding the first test series with variable O_2 ratios, it must be stated that the correlation between temperature and higher O_2 ratios could not be verified as predicted from the simulation. The trend in reality was reversed meaning with higher O_2 ratios lower temperatures were measured. This applies both to CH_4 and H_2. The main reason for this behaviour lies in the FFB design with its burner-stabilized flame. With lower O_2 ratios, the overall volume flow decreases leading to an earlier ignition point and a higher heat transfer to the burner plug. This results in a cooler flame temperature. Therefore it has to be said that the FFB is in this configuration not the right burner type to investigate higher O_2 ratios. To avoid this problem in the future, the lower N_2 volume flow in the oxidizer should be replaced with Ar which seems to be a promising way [28].

The influence of fuel showed a decent agreement with the simulation. The expected behaviour occured meaning the H_2 flame was cooler than the equivalent CH_4 flame. This is explained by the LBV which differs by a factor of 6 between both fuels. The higher LBV of H_2 causes a stronger upstream drive of the reaction zone which must end in a higher heat transfer to the burner plug. Therefore and as measured here, a cooler flame temperature must occur. In addition, the different temperature development along the vertical burner axis could be explained. In the simulation all

heat transfer mechanisms were intentionally disabled so that a comparability in higher HAB was only possible to a limited extent.

The addition of pure CO was also critically analyzed and it has to be outlined that future experiments investigating H_2 should target another species. The influence on the reaction kinetics is too high. H_2O lines seems to be a promising alternative to measure temperature [34]. Moreover, this molecule is the natural product of the elementary combustion reaction of H_2. However for CH_4, it was a perfect choice. It had a minimal effect on temperature but increased the CO species concentration so that the spectral absorbance could be pushed in a reasonable range.

Overall nevertheless, the results from the experiments and the simulations agreed well in particular for air flames. For higher O_2 ratios, the deviations increased but the backgrounds could be explained so that they can be prevented in the future.

Finally, the goals set could only be achieved with restrictions. But however, the data obtained in this work is valid and reliable which is expressed in the overall low uncertainty and good agreement with the simulation.

List of Figures

List of Tables

Bibliography

[1] dpa. "Energie: Verbandsstudie: Strom bleibt ohne russisches Gas teuer". In: *Die Zeit* (19.07.2023). URL: https://www.zeit.de/news/2023-07/19/verbandsstudie-strom-bleibt-ohne-russisches-gas-teuer (cit. on p. 1).

[2] Anil P. Nair, Daniel D. Lee, Daniel I. Pineda, Jason Kriesel, William A. Hargus, John W. Bennewitz, Stephen A. Danczyk, and R. Mitchell Spearrin. "MHz laser absorption spectroscopy via diplexed RF modulation for pressure, temperature, and species in rotating detonation rocket flows". In: *Applied Physics B* 126.8 (2020). ISSN: 0946-2171. DOI: 10.1007/s00340-020-07483-8 (cit. on pp. 1, 17, 26).

[3] Anil P. Nair, Nicolas Q. Minesi, Nicholas M. Kuenning, Alex R. Keller, and R. Mitchell Spearrin. "Optical pressure sensing at MHz rates via collisional line broadening of carbon monoxide: uncertainty quantification in reacting flows". In: *Applied Physics B* 129.4 (2023). ISSN: 0946-2171. DOI: 10.1007/s00340-023-07985-1 (cit. on pp. 1, 15, 17, 19, 26).

[4] David G. Goodwin, Harry K. Moffat, Ingmar Schoegl, Raymond L. Speth, and Bryan W. Weber. *Cantera: An Object-oriented Software Toolkit for Chemical Kinetics, Thermodynamics, and Transport Processes*. 2023. DOI: 10.5281/ZENODO.8137090 (cit. on pp. 3, 4, 30).

[5] University of Galway. *AramcoMech 2.0*. 20.09.2024. URL: https://www.universityofgalway.ie/combustionchemistrycentre/mechanismdownloads/aramcomech20/ (cit. on p. 4).

[6] Stanford University, SRI International. 20.09.2024. URL: https://web.stanford.edu/group/haiwanglab/FFCM2/ (cit. on p. 4).

[7] Gregory P. Smith, David M. Golden, Michael Frenklach, Nigel W. Moriarty, Boris Eiteneer, Mikhail Goldenberg, C. Thomas Bowman, Ronald K. Hanson, Soonho Song, William C. Gardiner Jr., Vitali V. Lissianski, and and Zhiwei Qin. *GRI-Mech 3.0*. 30.10.2002. URL: http://combustion.berkeley.edu/gri-mech/version30/text30.html (cit. on p. 4).

[8] Hamid Hashemi, Jakob M. Christensen, Sander Gersen, Howard Levinsky, Stephen J. Klippenstein, and Peter Glarborg. "High-pressure oxidation of methane". In: *Combustion and Flame* 172 (2016), pp. 349–364. ISSN: 00102180. DOI: 10.1016/j.combustflame.2016.07.016 (cit. on p. 4).

[9] University of California, San Diego. *SDmech*. 28.07.2018. URL: https://web.eng.ucsd.edu/mae/groups/combustion/mechanism.html (cit. on p. 4).

[10] M. D. Smooke, I. K. Puri, and K. Seshadri. "A comparison between numerical calculations and experimental measurements of the structure of a counterflow diffusion flame burning diluted methane in diluted air". In: *Symposium (International) on Combustion* 21.1 (1988), pp. 1783–1792. ISSN: 0082-0784. DOI: 10.1016/S0082-0784(88)80412-0. URL: https://www.sciencedirect.com/science/article/pii/S0082078488804120 (cit. on p. 4).

[11] Holthuis and Associates. *Flat Flame Burner - Burner Details*. 20.09.2024. URL: https://www.flatflame.com/about-flatflame (cit. on p. 8).

[12] P. N. Langenkamp. *Laser Diagnostics of Combustion-Generated Nanoparticles - Chapter 2*. 2018 (cit. on pp. 8, 10).

[13] S. Prucker, W. Meier, and W. Stricker. "A flat flame burner as calibration source for combustion research: Temperatures and species concentrations of premixed H2/air flames". In: *Review of Scientific Instruments* 65.9 (1994), pp. 2908–2911. ISSN: 0034-6748. DOI: 10.1063/1.1144637 (cit. on pp. 7, 32).

[14] *Combustion: Physical and Chemical Fundamentals, Modeling and Simulation, Experiments, Pollutant Formation*. 4th Edition. SpringerLink Bücher. Berlin, Heidelberg: Springer-Verlag Berlin Heidelberg, 2006. ISBN: 9783540453635. DOI: 10.1007/978-3-540-45363-5 (cit. on p. 9).

[15] Raymond Friedman. "Experimental Flame Research: Flame Structure . R. M. Fristrom and A. A. Westenberg. McGraw-Hill, New York, 1965. xiv + 424 pp. Illus. $17.50". In: *Science* 150.3704 (1965), pp. 1703–1704. ISSN: 0036-8075. DOI: 10.1126/science.150.3704.1703 (cit. on p. 9).

[16] S. Mathur, P. K. Tondon, and S. C. Saxena. "Thermal conductivity of binary, ternary and quaternary mixtures of rare gases". In: *Molecular Physics* 12.6 (1967), pp. 569–579. ISSN: 0026-8976. DOI: 10.1080/00268976700100731 (cit. on p. 10).

[17] R. J. Kee, Michael Elliott Coltrin, Peter Glarborg, and Huayang Zhu. *Chemically reacting flow: Theory, modeling, and simulation*. Second edition. Hoboken NJ: John Wiley & Sons, 2017. ISBN: 9781119186281 (cit. on p. 10).

[18] Ronald K. Hanson, Christopher S. Goldenstein, and R. Mitchell Spearrin. *Spectroscopy and Optical Diagnostics for Gases*. 1st ed. 2016. Cham: Springer International Publishing and Imprint: Springer, 2016. ISBN: 9783319232522 (cit. on pp. 10–13, 15, 16).

[19] Nicholas M. Kuenning, Anil P. Nair, Alex R. Keller, Nicolas Q. Minesi, Emre Ozen, Blaine Bigler, Jason Kriesel, John W. Bennewitz, Jason Burr, Stephen A. Danczyk, and R. Mitchell Spearrin. "Multiplexed MHz-rate mid-infrared laser absorption spectroscopy for simultaneous in-chamber CO, CO2, H2O, temperature, and pressure in a rotating detonation rocket engine". In: *Combustion and Flame* 268 (2024), p. 113608. ISSN: 00102180. DOI: 10.1016/j.combustflame.2024.113608 (cit. on pp. 12, 15, 17, 26, 27).

[20] Lemthong Lathdavong, Jie Shao, Pawel Kluczynski, Stefan Lundqvist, and Ove Axner. "Methodology for detection of carbon monoxide in hot, humid media by telecommunication distributed feedback laser-based tunable diode laser absorption spectrometry". In: *Applied optics* 50.17 (2011), pp. 2531–2550. DOI: 10.1364/AO.50.002531 (cit. on p. 13).

[21] Robert R. Gamache, Bastien Vispoel, Michaël Rey, Andrei Nikitin, Vladimir Tyuterev, Oleg Egorov, Iouli E. Gordon, and Vincent Boudon. "Total internal partition sums for the HITRAN2020 database". In: *Journal of Quantitative Spectroscopy and Radiative Transfer* 271 (2021), p. 107713. ISSN: 00224073. DOI: 10.1016/j.jqsrt.2021.107713 (cit. on p. 16).

[22] I. E. Gordon, L. S. Rothman, R. J. Hargreaves, R. Hashemi, E. V. Karlovets, F. M. Skinner, E. K. Conway, C. Hill, R. V. Kochanov, Y. Tan, P. Wcisło, A. A. Finenko, K. Nelson, P. F. Bernath, M. Birk, V. Boudon, A. Campargue, K. V. Chance, A. Coustenis, B. J. Drouin, J.–M. Flaud, R. R. Gamache, J. T. Hodges, D. Jacquemart, E. J. Mlawer, A. V. Nikitin, V. I. Perevalov, M. Rotger, J. Tennyson, G. C. Toon, H. Tran, V. G. Tyuterev, E. M. Adkins, A. Baker, A. Barbe, E. Canè, A. G. Császár, A. Dudaryonok, O. Egorov, A. J. Fleisher, H. Fleurbaey, A. Foltynowicz, T. Furtenbacher, J. J. Harrison, J.–M. Hartmann, V.–M. Horneman, X. Huang, T. Karman, J. Karns, S. Kassi, I. Kleiner, V. Kofman, F. Kwabia–Tchana, N. N. Lavrentieva, T. J. Lee, D. A. Long, A. A. Lukashevskaya, O. M. Lyulin, V.Yu. Makhnev, W. Matt, S. T. Massie, M. Melosso, S. N. Mikhailenko, D. Mondelain, H.S.P. Müller, O. V. Naumenko, A. Perrin, O. L. Polyansky, E. Raddaoui, P. L. Raston, Z. D. Reed, M. Rey, C. Richard, R. Tóbiás, I. Sadiek, D. W. Schwenke, E. Starikova, K. Sung, F. Tamassia, S. A. Tashkun, J. Vander Auwera, I. A. Vasilenko, A. A. Vigasin, G. L. Villanueva, B. Vispoel, G. Wagner, A. Yachmenev, and S. N. Yurchenko. "The HITRAN2020 molecular spectroscopic database". In: *Journal of Quantitative Spectroscopy and Radiative Transfer* 277 (2022), p. 107949. ISSN: 00224073. DOI: 10.1016/j.jqsrt.2021.107949 (cit. on p. 16).

[23] Nicolas Q. Minesi, Miles O. Richmond, Christopher C. Jelloian, Nicholas M. Kuenning, Anil P. Nair, and R. Mitchell Spearrin. "Multi-line Boltzmann regression for near-electronvolt temperature and CO sensing via MHz-rate infrared laser absorption spectroscopy". In: *Applied Physics B* 128.12 (2022). ISSN: 0946-2171. DOI: 10.1007/s00340-022-07931-7 (cit. on pp. 16, 26).

[24] Christopher C. Jelloian, Nicolas Q. Minesi, and R. Mitchell Spearrin. "High-speed mid-infrared laser absorption spectroscopy of CO 2 for shock-induced thermal non-equilibrium studies of planetary entry". In: *Applied physics. B, Lasers and optics* 128.12 (2022), p. 216. ISSN: 0946-2171. DOI: 10.1007/s00340-022-07934-4 (cit. on p. 17).

[25] A. B. McLean, C.E.J. Mitchell, and D. M. Swanston. "Implementation of an efficient analytical approximation to the Voigt function for photoemission lineshape analysis". In: *Journal of Electron Spectroscopy and Related Phenomena* 69.2 (1994), pp. 125–132. ISSN: 0368-2048. DOI: 10.1016/0368-2048(94)02189-7. URL: https:

//www.sciencedirect.com/science/article/pii/0368204894021897 (cit. on p. 18).

[26] Christopher S. Goldenstein, R.Mitchell Spearrin, Jay. B. Jeffries, and Ronald K. Hanson. "Infrared laser-absorption sensing for combustion gases". In: *Progress in Energy and Combustion Science* 60 (2017), pp. 132–176. ISSN: 03601285. DOI: 10.1016/j.pecs.2016.12.002 (cit. on p. 21).

[27] L. S. Rothman, I. E. Gordon, R. J. Barber, H. Dothe, R. R. Gamache, A. Goldman, V. I. Perevalov, S. A. Tashkun, and J. Tennyson. "HITEMP, the high-temperature molecular spectroscopic database". In: *Journal of Quantitative Spectroscopy and Radiative Transfer* 111.15 (2010), pp. 2139–2150. ISSN: 00224073. DOI: 10.1016/j.jqsrt.2010.05.001 (cit. on p. 26).

[28] D. L. Zhu, F. N. Egolfopoulos, and C. K. Law. "Experimental and numerical determination of laminar flame speeds of methane/(Ar, N2, CO2)-air mixtures as function of stoichiometry, pressure, and flame temperature". In: *Symposium (International) on Combustion* 22.1 (1989), pp. 1537–1545. ISSN: 0082-0784. DOI: 10.1016/S0082-0784(89)80164-X. URL: https://www.sciencedirect.com/science/article/pii/S008207848980164X (cit. on pp. 29, 36).

[29] J. P. Botha and D. B. Spalding. "The laminar flame speed of propane/air mixtures with heat extraction from the flame". In: (1954) (cit. on p. 29).

[30] A. V. Sepman, A. V. Mokhov, and H. B. Levinsky. "Extending the predictions of chemical mechanisms for hydrogen combustion: Comparison of predicted and measured flame temperatures in burner-stabilized, 1-D flames". In: *International Journal of Hydrogen Energy* 36.15 (2011), pp. 9298–9303. ISSN: 03603199. DOI: 10.1016/j.ijhydene.2011.04.198 (cit. on p. 30).

[31] Hans Dieter Baehr and Karl Stephan. *Wärme- und Stoffübertragung*. 8th ed. 2013. Berlin Heidelberg: Springer Berlin Heidelberg and Imprint: Springer Vieweg, 2013. ISBN: 9783642365584 (cit. on p. 30).

[32] Xinyu Yang, Zhimin Peng, Yanjun Ding, and Yanjun Du. "Temperature and OH concentration measurements by ultraviolet broadband absorption of OH(X) in laminar methane/air premixed flames". In: *Fuel* 288 (2021), p. 119666. ISSN: 00162361. DOI: 10.1016/j.fuel.2020.119666 (cit. on p. 32).

[33] P. Weigand, R. Lückerath, and W. Meier. "Documentation of Flat Premixed Laminar CH4/Air Standard Flames: Temperatures and Species Concentrations". In: () (cit. on p. 32).

[34] Fabio A. Bendana, Isabelle C. Sanders, Josue J. Castillo, China G. Hagström, Daniel I. Pineda, and R. Mitchell Spearrin. "In-situ thermochemical analysis of hybrid rocket fuel oxidation via laser absorption tomography of $$\text CO$$, $$\text CO_2$$, and $$\text H_2\text O$$". In: *Experiments in Fluids* 61.9 (2020). ISSN: 0723-4864. DOI: 10.1007/s00348-020-03004-7 (cit. on p. 37).